Simulation of the refuelling process for an LH_2-powered commercial aircraft part 1 - Modelling and validation

ten Damme, L.; van Put, M.; Gangoli Rao, A.

DOI
10.1016/j.ijhydene.2025.152168

Publication date
2025

Document Version
Final published version

Published in
International Journal of Hydrogen Energy

International Journal of Hydrogen Energy 195 (2025) 152168

Contents lists available at ScienceDirect

International Journal of Hydrogen Energy

journal homepage: www.elsevier.com/locate/he

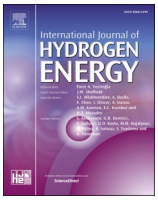

Simulation of the refuelling process for an LH_2-powered commercial aircraft part 1 - Modelling and validation

L. ten Damme [a], M. van Put [b], A. Gangoli Rao [a,*]

[a] Faculty of Aerospace Engineering, Delft University of Technology, The Netherlands
[b] Airbus Netherlands B.V, The Netherlands

A B S T R A C T

Liquid hydrogen (LH_2) is a promising candidate for zero emission aviation, but its cryogenic properties make the refuelling process fundamentally different from that of conventional jet fuels. Although previous studies have addressed LH_2 storage and system integration, detailed modelling of the refuelling process remains limited.

This paper presents the first part of a two-part study focused on simulation of the refuelling process for an LH_2-powered commercial aircraft. An existing tank model is substantially modified to more accurately capture relevant physical phenomena, including heat transfer and droplet dynamics during top-fill spray injection. Newly available experimental data on LH_2 no-vent filling enables direct validation of the model under conditions that match the experimental setup.

A sensitivity analysis identifies the most influential parameters that affect model precision, including loss coefficient, droplet diameter, radiative heat ingress, and vent-closing pressure. The validated model forms the basis for Part 2 of this study, in which it is applied to a representative LH_2-powered commercial aircraft to simulate refuelling times, quantify venting losses, and assess the impact of key operational settings. These results support the design of efficient LH_2 refuelling systems for future aircraft and airport infrastructure.

Nomenclature

Abbreviations	
Al	aluminium
avg	average
ET	external tank
GFSSP	Generalized Fluid System Simulation Package
GH_2	gaseous hydrogen
LH_2	liquid hydrogen
MAE	mean absolute error
MLI	multilayer insulation
NBP	natural boiling point
NVF	no vent fill
ODE	ordinary differential equation
REFPROP (NIST)	Reference Fluid Thermodynamic and Transport Properties Database
ST	stationary length

Symbols

α_v	valve friction parameter	$\sqrt{kg.m}$
$\alpha_{\lambda tr}$	transfer line valve coefficient	[−]
α	convective heat transfer coefficient	$\frac{W}{m^2K}$
β	thermal expansion coefficient	$\frac{1}{K}$
ϵ_{tr}	roughness of the transfer line	m
α_{eff}	effective friction parameter	$\sqrt{kg.m}$
α_{pipe}	pipe friction parameter	$\sqrt{kg.m}$
γ	ratio of specific heats	[−]
κ	thermal conductivity	w/mK
λ	valve state	–
μ_f	friction coefficient	–
μ	dynamic viscosity	Pa·s
ν	kinematic viscosity	$\frac{m^2}{s}$
τ	time constant	s
$\%fill$	fill fraction	–
Δt	grid time constant	s
Q	rate of heat transfer	W
W	rate of work	W
$\mathbf{u}$	array containing specific internal energy values for each layer of the bulk liquid or vapour	
ρ	density	$\frac{kg}{m^3}$
c_p	specific heat capacity at constant pressure	$\frac{J}{kg \cdot k}$
c_v	specific heat capacity at constant volume	$\frac{J}{kg \cdot k}$
c_{vap}	vaporiser valve flow coefficient	[−]
c_w	temperature dependent specific heat capacity	$\frac{J}{K}$
$D_{\lambda tr}$	transfer line valve diameter	m
D	diameter	m

(continued on next column)

(continued)

(continued on next page)

* Corresponding author.
E-mail address: a.gangolirao@tudelft.nl (A. Gangoli Rao).

https://doi.org/10.1016/j.ijhydene.2025.152168
Received 28 September 2024; Received in revised form 4 September 2025; Accepted 21 October 2025
Available online 12 November 2025

(*continued*)

$f(.)$	function of	
g	free-fall acceleration due to gravity	$\frac{m}{s^2}$
H_0	height at the interface between the liquid and the vapour	m
H	height	m
h	specific enthalpy	$\frac{J}{kg \cdot K}$
J	mass flow rate	kg/s
K	loss coefficient	–
L	length	m
m	mass	kg
N	grid size	–
n	dimensionless exponent for saturated hydrogen vapour	–
p_c	critical pressure	Pa
Pr	Prandtl number	–
p	pressure	bar
$\dot{q}''$	heat flux	$\frac{W}{m^2}$
Q	vapour quality	–
$r_{top-to-bottom}$	ratio between top and bottom fill	–
Ra	Rayleigh number	–
Re	Reynolds number	–
r	radius	m
$S_{\lambda tr}$	transfer line valve cross-sectional area	m^2
S	area	m^2
T_s	temperature of the saturated film	K
T_c	critical temperature	K
t_{final}	final time of the interval of integration	s
T	temperature	K
u	specific internal energy	$\frac{J}{kg \cdot K}$
V	volume	m^3
v	velocity	$\frac{m}{s}$

Subscripts

0	initial condition
atm	atmospheric conditions
avg	average
boil	boiling after the vaporiser
cd	condensation
cond	conduction
conv	convection
el	from the environment to the liquid phase
ET	external tank
ev	from the environment to the vapour phase
ew	from the environment to the tank wall
f	fluid
$l+v$	liquid and vapour
l,v	*interface* interface between the liquid and the vapour phase
l	liquid *max* maximal
ST	stationary tank or supply
tot	total
tr	transfer line
vap	vaporisation
vent	vent line
V	vapour
W	tank wall

1. Introduction

Technological innovations in aircraft, such as lighter materials, better engines, improved aerodynamics, etc., have resulted in a reduction of 70 % in passenger-km consumption since the beginning of the jet age in 1960 [1]. However, despite the significant reduction in aircraft passenger km consumption over the past several decades, the contribution of commercial aviation to global greenhouse gas emissions is increasing and this growth has not yet been stabilised with the current state of technological advancements. In 2018 – just before the COVID pandemic – commercial aviation contributed to 2.4 % of global CO_2 emissions from fossil fuel use [2]. This might be considered insignificant, but with the projected future growth of aviation, these emissions and their influence on the health and well-being of the public and the environment can be substantial [3]. In addition, research indicates that a significant part of aviation's climate impact is due to non-CO_2 emissions. If no mitigation actions are taken, it is highly probable that aviation alone will contribute to a temperature increase of 0.1 °C by 2050 [4]. The Paris Agreement - which came into effect on December 4, 2016 - prescribes that the emission of greenhouse gases from the aviation industry must be net zero in 2050 to keep global warming below 1.5 °C.

The passenger market demonstrates that the revenue passenger kilometres (RPKs) grow at an average annual rate of 3.6 % for both domestic and international demand from 2018 to 2050 (using the midCOVID-19 recovery scenario). The worldwide freight tonne kilometres (FTKs) forecast is expected to increase by 3.5 % annually, while the international FTKs forecast are expected to expand by 3.4 % annually [5]. This projected growth underscores the urgent need to innovate and introduce new aircraft into the commercial aviation sector in order to reduce its environmental impact. New technologies have already been broadly investigated in previous research. Liquid hydrogen (LH_2) is a promising alternative fuel for commercial aircraft due to its high energy density and low emissions. The use of LH_2 as fuel has the potential to significantly reduce carbon emissions and help combat climate change [6].

Since the 1970s, studies have been carried out on the overall impact of LH_2 on airport infrastructure and aircraft design [7,8]. The main aspects of the fuel system, fuel containment system, engine characteristics, and aircraft characteristics have been identified, as well as their operating conditions. However, the modelling process and method have not been shown.

The natural boiling point (NBP) of hydrogen is extremely low cryogenic temperatures, namely at 20.4 K or −252.8 °C. Due to both the cryogenic temperature and the inherent properties of hydrogen, the fuelling process for an LH_2 powered aircraft is significantly different compared to Kerosene. The refuelling process for LH_2 is of concern, since it has the potential to significantly impact the economic feasibility of future aircraft [9]. However, a detailed analysis of the refuelling process has received little attention in the literature.

Recently, Mangold et al. [10] presented the boundary conditions, calculation methods, and analysis of the refuelling system. It is concluded that the LH_2 refuelling procedure does not have a negative impact on the aircraft turnaround times. An LH_2 refuelling rate of 20 kg/s is considered based on assuming the same energy flow as for an equivalent Kerosene aircraft to obtain the same refuelling time. However, this assumption is in contradiction to the Clean Hydrogen Joint Agreement [11], which assumes the same flow rate of LH_2 as an equivalent Kerosene aircraft, resulting in 1–3 times longer refuelling times (depending on the range of the aircraft).

The primary focus of this research is to simulate the refuelling process, specifically by using detailed numerical modelling, to understand the thermal aspects involved during the process. Unlike preliminary calculations, which may lack precision, a comprehensive and accurate model can significantly impact the design of the refuelling process. By reducing flow fluctuation, pressure oscillations, and irrational safety considerations, a precise thermodynamic model can lead to the development of lighter systems and consequently more fuel-efficient aircraft [12].

This paper constitutes the first part of a two-part study on the numerical simulation of LH_2 refuelling for commercial aircraft. The primary objective of Part 1 is to establish a methodology for simulating LH_2 transfer and to validate the resulting model using experimental data. The model development and validation approach is presented, incorporating key physical phenomena such as heat transfer and droplet evaporation.

Part 2 applies the validated model to a representative case study of a future LH_2-powered commercial aircraft. The focus is on quantifying refuelling times, evaluating venting losses, and performing a sensitivity analysis of key operational parameters. By distinguishing between

model development and validation (Part 1) and practical application to a case study (Part 2), this two-part approach aims to provide both a rigorous numerical modelling framework and practical insights to inform future aircraft design and airport operations.

2. Literature review

The objective of the literature study is to determine the most suitable numerical model that can be validated against experimental data available in the literature.

2.1. Numerical models in literature

The Generalized Fluid System Simulation Package (GFSSP) [13] and SINDA/FLUINT [14] are two of the most widely used thermal/fluid codes to design, analyse and research systems that could experience cryogenic two-phase flow. For modelling heat transfer and fluid flow in large multicomponent systems like feed systems, spacecraft, and propellant tanks, these programmes are preferred. However, their accuracy is limited: Hartwig et al. [15] assess how well those correlations perform in predicting cryogenic flow boiling in pipe quenching (or rapid cooling) experiments. The two-phase correlations used in SINDA/FLUINT and GFSSP indicate large mean absolute errors (MAE) with data from cryogenic quenching.

As GFSSP and SINDA/FLUINT are considered unsuitable for modelling the LH_2 refuelling process, more research is performed. The work of Al Ghafri et al. [16] and the work of Petitpas [17] are found to be the only models developed for simulating LH_2 behaviour in tanks.

The model from Al Ghafri et al. [16]. includes realistic heat transfer mechanisms, takes into account heat transfer from the vapour to the liquid phase, and calculates thermodynamic properties using reference equations of state. However, this work considers only the boil-off behaviour of a static tank and, therefore, does not consider a refuelling case. In addition, chill down is not considered. This model is equipped with an easy-to-use user interface and can be downloaded for free, which is a big advantage. However, it is not possible to analyse and modify the source code, which implies that it is not possible to add or modify features and, therefore, is not considered suitable.

Osipov et al. [18] develop a two-fluid model to simulate the complex heat transfer modes that occur during LH_2 rocket propellant loading. This model considers the dynamic process of condensation and vaporisation due to conduction and convection between the saturated film and the vapour and liquid volumes by using dynamic equations. The thermodynamic states of hydrogen are described by the ideal gas equations of state. NASA [19] implements this model in MATLAB to perform simulations, which is published as open-source. Petitpas [17, 20] uses this MATLAB model as the basis for an LH_2 transfer model. The LH_2 pathway considered in the study consists of a large storage tank at the liquefaction plant, a fuel tanker that transports LH_2 from the liquefaction plant to the fuel station and the fuel tank at the fuel station. Petitpas [17] improves the accuracy of the model of NASA in several ways. First, hydrogen is considered as a real gas instead of an ideal one. In addition, the state properties of the MATLAB code are now coupled to a thermodynamic REFPROP database to improve accuracy. Then, for both the supply and receiving vessels, equations are added to simulate changes in temperature in the bulk liquid phases.

Next, the specific heat of the vessel's wall is assumed to have a constant thermal inertia when the code is first written. To account for the changing specific heat capacity, this term is modified to change as a function of temperature. In addition, the ability to supply LH_2 through the top of a vertical cryogenic tank is included. However, the physics behind LH_2 droplet vaporisation in a cryogenic vapour environment is found to be quite complex. Therefore, a relatively straightforward strategy is chosen in which only a small portion of the LH_2 can be fed into the top of the receiving vessel which vaporises and contributes to the mass and energy balances of the vapour control volume [17]. Therefore, significant top filling is likely to require additional modifications in order to be simulated properly.

The model of Petitpas [20] is transient but has no spatial dependency. Therefore, the temperature distribution is not taken into account (other than the nodes in the vapour and liquid on both sides of the saturated film). Additionally, the model does not consider the effects of flashing within the transfer line, nor does it account for the thermal mass or imperfect insulation of the transfer line. Then, the wall of the vessel is considered to have a uniform temperature. Next, it is assumed that the trailer is used sufficiently frequently and that the bulk fluid temperature is moderately low and stable. As a result, the wall of the trailer is not given any thermal mass.

In addition, while the original NASA [19] model considers modelling the thermal stratification in the fuel tank [21], it is not kept in Petitpas' [20] tank model. However, it is assumed that the duration in which the refuelling process is completed is much shorter than the timescale required for (significant) thermal stratification.

Moreover, no para-ortho conversion is considered, which is justified by the typically low temperatures and short timescales. Petitpas [20] considers 100 % parahydrogen, which is considered valid as at the NBP of hydrogen, the equilibrium composition is 99.8 % parahydrogen. However, it is stated that experimental measurements are required to confirm the relevance of the approach and validate the MATLAB code presented in Ref. [17].

Despite these limitations, this tank model from Petitpas [20] is considered promising as a basis for the numerical simulation of the LH_2 refuelling process, as the source code can be analysed and modified as it is published open source. A schematic representation of Petitpas' [20] tank model is shown in Fig. 1.

In summary, Petitpas' [20] tank model is a simplified lumped parameter approach based on fundamental conservation laws, capable of modelling multiphase mass and energy transfer, including dynamic condensation, vaporisation and tank pressurisation. A tank model flow chart, based on the work of Petitpas [20], is displayed in Fig. 2. The transient problem is resolved using an ordinary differential equation (ODE) solver, indicated by the red block in the figure. This ODE solver requires as input the initial state variables and the state derivatives, which are indicated by the set of blue and yellow blocks, respectively. The green block indicates that when the ET vent valve changes state (open ↔ closed), the ODE solver stops. Each block of this flow chart is discussed in detail in Appendix A.

2.2. Experimental data from literature

The objective of the paper is to find a methodology to simulate LH_2 transfer and validate it with experimental data. Hartwig et al. [22] performed LH_2 transfer tests on a thin-walled flightweight aluminium (Al) tank, which are performed at the NASA Glenn Research Center. According to Hartwig et al. [22]: "*Up to this point in the historical literature, the chilldown and fill process had never been optimised to conserve time.*" To determine whether the rapid chill-down and fill method, followed by a no-vent fill (NVF), is feasible, four tests are carried out.

The study consists of four tests, each of which includes a tank evacuation phase (during which the tank is pumped down to vacuum), a vented chill-down phase (during which the tank is chilled down with the vent valve open), and a NVF phase. Each test considers LH_2 as the transfer fluid. Although the chill-down conditions for all four tests are the same, there are some differences in the NVF phase parameters, such as the initial fill level of the receiving tank (RT) and the initial mass averaged wall temperature of the RT.

The supply tank (ST) has a capacity of 5.678 m^3 and a maximum expected operating pressure of 4.14 bar. The supply tank is connected to the receiving tank (RT) using a vacuum-jacketed supply line that has a diameter of 2.54 cm and contains pressure taps that open an inline emergency relief valve when pressure exceeds 5.17 bar.

The RT is a spherical aluminium flight weight tank, depicted in

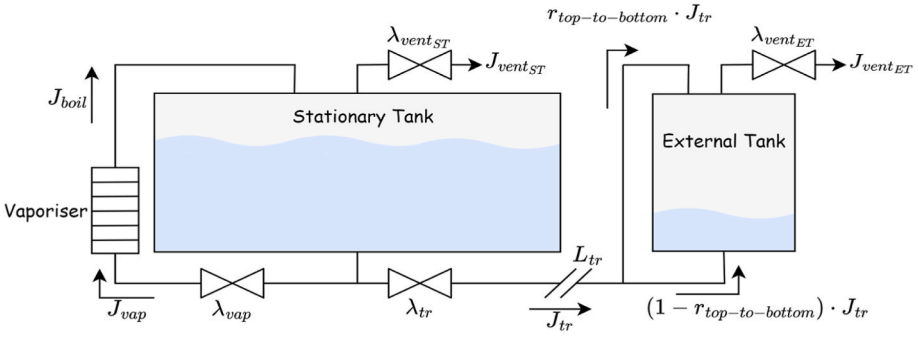

Fig. 1. Schematic representation based on Petitpas' [20] tank model.

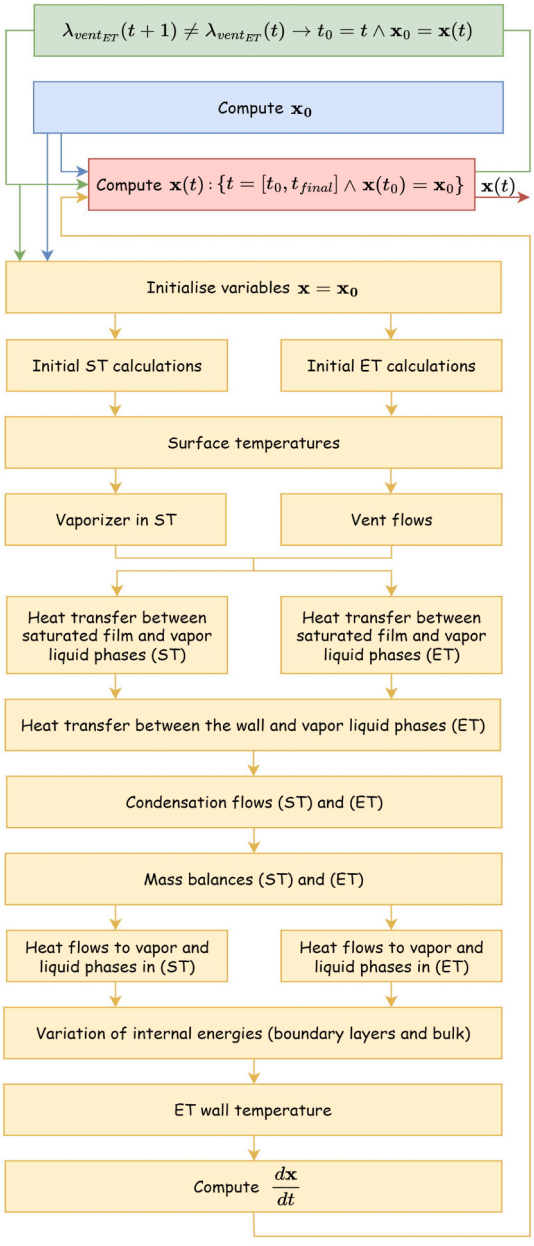

Fig. 2. Flowchart of the tank model by Petitpas [20].

Fig. 3. Aluminium receiver tank [22].

Fig. 3. The tank has a mass of 40.37 kg, with a wall thickness of 1 mm and an exterior diameter of 1.372 m. The tank can store up to 1.39 m^3 fluid. It is designed to withstand a proof pressure of 6.21 bar and a maximum allowed working pressure of 4.46 bar. To reduce heat leakage into the RT during testing, the tank is suspended inside a cylindershaped vacuum chamber. A spray bar is used to inject liquid into the receiving tank.

The fourth test is found to be the optimal rapid ventilated chill and fill method, achieving the necessary fill level quickly and without encountering any significant technical issues due to sensors, operator error, etc. The test matrix for this fourth test is shown in Table 1.

Due to the cooling of the transfer line, the two-phase flow always persists throughout the initial phases of the transfer process, making it impossible to determine the flow's entrance condition. The equation for the average wall temperature (avg) is shown in Eq. (1).

$$T_{avg} = \frac{\sum_{i=1}^{n} T_i \Delta m_i + T_{lid} m_{lid}}{m_{RT} + m_{lid}} \tag{1}$$

The results of Test 4 are shown in Fig. 4.

The purpose of the experimental data is to use them to validate the capability of Petitpas' [20] tank model to simulate the actual refuelling phase after the system is chilled down. First, the parameters used in the experimental setup, such as tank material and dimensions, must be

Table 1
Test matrix for Test 4 from the experiment conducted by Hartwig et al. [22].

Phase	Time	Variable	Value	Unit
Chill-down	Start	Time	40	s
		RT pressure	0.2184	bar
		RT ullage temperature	285.1	K
		Mass average RT temperature	278.66	K
		RT lid temperature	285.15	K
	During	Avg inlet pressure	2.1142	bar
		Avg inlet temperature	25.94	K
NVF	Start	Time	179	s
		Mass flow rate	0.41	$\frac{kg}{s}$
		RT pressure	1.164	bar
		RT ullage temperature	20.86	K
		RT liquid temperature	20.98	K
		Mass vapour	0.67	kg
		Mass liquid	36.75	kg
		Liquid level	45	% fill
		Mass averaged RT temperature	32.77	K
		RT lid temperature	125.33	K
	During	Avg inlet pressure	2.3387	bar
		Avg inlet temperature	25.94	K
	Final	Time	338	s
		RT pressure	1.4569	bar
		RT ullage temperature	21.48	K
		RT liquid temperature	21.84	K
		Mass vapour	0.12	kg
		Mass liquid	87.75	kg
		Liquid level	91	% fill
		Mass averaged RT temperature	24.6	K
		RT lid temperature	40.05	K

translated into the Petitpas' [20] tank model, as well as the initial conditions of the NVF phase, as shown in Table 1.

Although the final values in Table 1 can be compared fairly easily, the transient data must be obtained from Fig. 4, which is expected to be less accurate. A comparison between the experimental data and the numerical model at the end of the NVF process is presented later in this paper in Table 5.

2.2.1. Limitations

By comparing the transient behaviour during the NVF test, as shown in Fig. 4, with the final parameters at the end of the NVF test at $t = 338$ s, it is immediately observed that the transient data is not displayed between $t = 320$ s and $t = 338$ s. Therefore, it is considered that the comparison between the experiment and the model could show discrepancies.

Another observation is made by considering the pressure in the receiver tank. Until around $t = 307$ s, the pressure in the RT increases to a maximum value of 3.345 bar. However, later, the pressure decreases to 3.18 bar, followed by some oscillating behaviour. The decrease in pressure is unexpected, as the no-vent fill test implies that the vent valve in the RT stays closed during the filling process.

Especially when considering the pressure at the end of the NVF process at $t = 338$ s in Table 1, the pressure is decreased to an even lower value of 1.46 bar. Therefore, it is predicted that after $t = 307$ s, the vent valve opens, causing pressure to decrease.

3. Tank model modification and validation

While Petitpas' [20] original tank model is based on physical

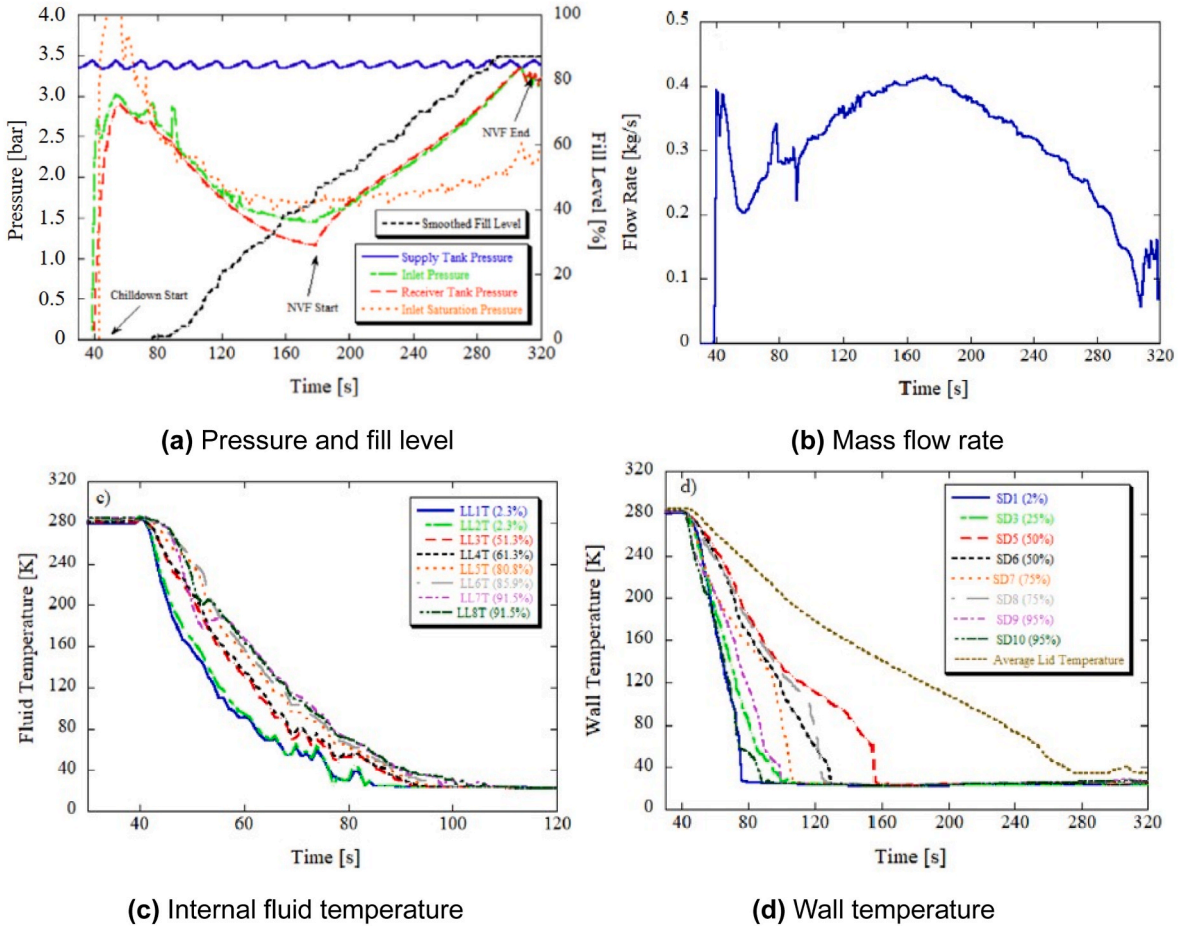

Fig. 4. Results of test 4 in the RT [22].

principles, the model was unable to accurately simulate the refuelling behaviour observed in Test 4 of the experiments by Hartwig et al. [22]. Therefore, this section aims to outline the modifications carried out and the validation of the modified tank model for the no-vent filling (NVF) case.

One of the key modifications involves the implementation of a spray model to replicate the spray bar used in the experimental setup. In addition, a sensitivity analysis is conducted to identify the model parameters that best align with the experimental data, based on comparisons of the fill level, receiver tank pressure, and transfer line mass flow rate.

3.1. Implementation in Python

First, Petitpas' [20] tank model is rewritten from MATLAB to Python code. MATLAB's stiff *ode15s* solver is replaced by Scipy's *solve_ivp* solver, using the *BDF* integration method, as this method is suitable for solving stiff ODEs.

3.2. Modifications to the numerical model

Fig. 5 shows a schematic representation of the LH_2 transfer pathway from the supply tank, through a transfer line, to the receiving tank, as used in the experiment. Compared to the schematic based on the Petitpas' [20] tank model, shown in Fig. 1, this set-up differs in the way LH_2 enters the receiving tank and the geometry of both tanks.

The following sections provide a detailed description of the modifications introduced to enhance the accuracy of the model.

3.2.1. Heat transfer correlations

Lloyd and Moran [23] present a correlation for the Nusselt number describing natural convection adjacent to horizontal surfaces in both laminar and turbulent regimes, as shown in Eq. (2) and Eq. (3), respectively. These correlations are used to determine the heat transfer between the saturated film and the liquid and vapour phases. Although these correlations are well known in the open literature and are also used in the original NASA model [19], Petitpas' [20] tank model does not consider these. Therefore, the correlations of Lloyd and Moran are preferred. Furthermore, flow over the spherical tank wall is considered free convection over a vertical plate, since the liquid flows mostly in the vertical direction during refuelling. Churchill and Chu [24] developed a correlation for the Nusselt number for the free laminar and turbulent convection over a vertical plate, displayed in Eq. (4) and Eq. (5) respectively. Compared to Petitpas' [20] tank model, it is preferred to use the correlation of Churchill and Chu since a distinction is made between laminar and turbulent flow, and the correlations are considered well known in open literature, which is not the case for the correlations used in Petitpas' [20] tank model.

$$Nu = 0.54 Ra^{\frac{1}{4}}, 10^4 < Ra < 10^7 \tag{2}$$

$$Nu = 0.15 Ra^{\frac{1}{3}}, 10^7 < Ra < 10^9 \tag{3}$$

$$Nu = 0.68 + \left(\frac{0.670 \cdot Ra^{\frac{1}{4}}}{\left[1 + \left(\frac{0.492}{Pr}\right)^{\frac{9}{16}}\right]^{\frac{4}{9}}} \right), 10^5 < Ra < 10^9 \tag{4}$$

$$Nu = 0.825 + \left(\frac{0.387 \cdot Ra^{\frac{1}{6}}}{\left[1 + \left(\frac{0.492}{Pr}\right)^{\frac{9}{16}}\right]^{\frac{8}{27}}} \right), Ra > 1 \cdot 10^9 \tag{5}$$

3.2.2. Friction factor

It is considered to modify the friction factor μ_f used as a function of the Re number instead of assuming it to be constant. Usually, the friction factor for turbulent flow pipes or ducts is approximated using the Colebrook-White equation. However, the Colebrook equation can only be used to model turbulent flow in pipes when the Re number is higher than $Re \approx 4000$ [25].

As the refuelling flow rate and thus the Re number are low close to the start and end of the refuelling process, it is desired to obtain a relation that is also capable of accurately predicting the low friction coefficient Re numbers. Churchill's [26] equation, as displayed in Eq. (6), is able to compute the friction factor for both high- and very slow-flow ($Re < 1$) Re numbers, and is therefore preferred.

$$\mu_f = 8 \cdot \left[\left(\frac{8}{Re}\right)^{12} + \frac{1}{\left(\left[2.457 \cdot ln\left(\left(\frac{7}{Re}\right)^{0.9} + 0.27 \cdot \left(\frac{\epsilon}{D}\right) \right) \right]^{16} + \left[\frac{37530}{Re}\right]^{16} \right)^{\frac{3}{2}}} \right]^{\frac{1}{12}} \tag{6}$$

3.2.3. REFPROP versus empirical relations

Petitpas' [20] tank model occasionally uses correlations to determine thermophysical properties instead of retrieving them directly from REFPROP. These correlations were derived from REFPROP version 9.1. The first advantage is that the computational cost of using a correlation is significantly lower compared to using REFPROP in every iteration [27]. Secondly, some properties, like the liquid temperature and density as functions of internal energy, are not directly accessible in REFPROP but can be determined using correlations. However, it is important to

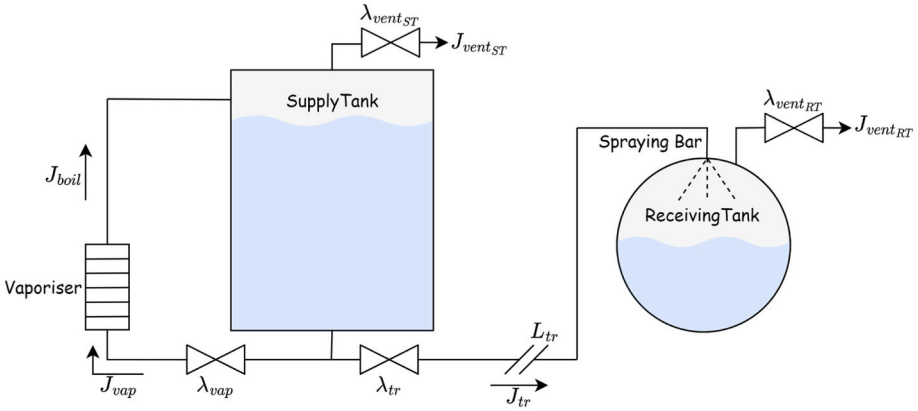

Fig. 5. Schematic of the LH_2 transfer between supply and receiving tank of the experimental set-up.

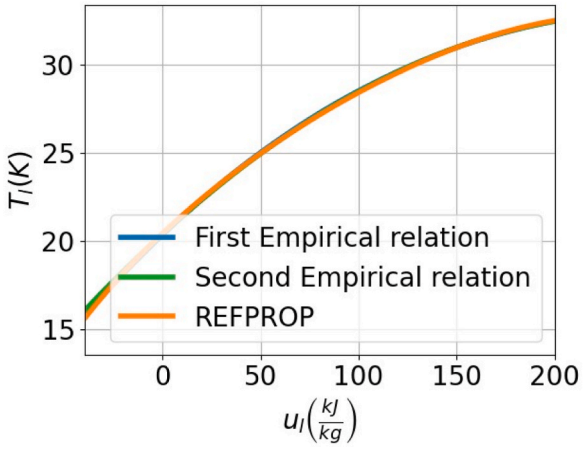

(a) Liquid temperature versus internal energy

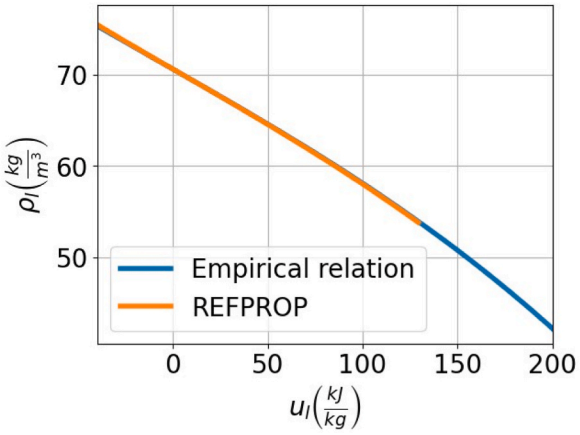

(b) Liquid density versus internal energy

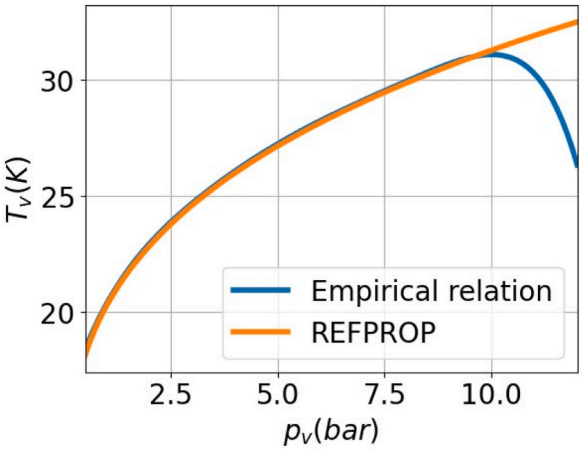

(c) Saturated vapour temperature versus

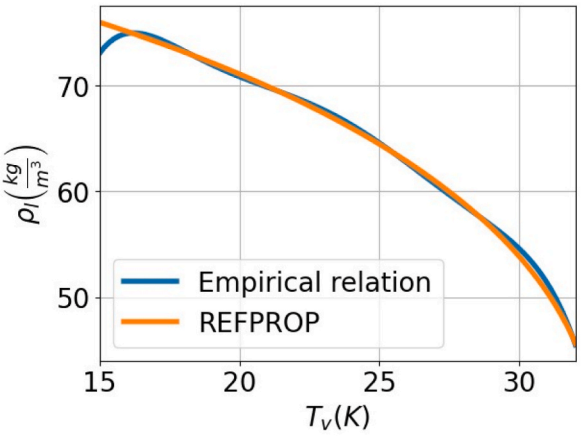

(d) Saturated liquid density versus vapour pressure temperature

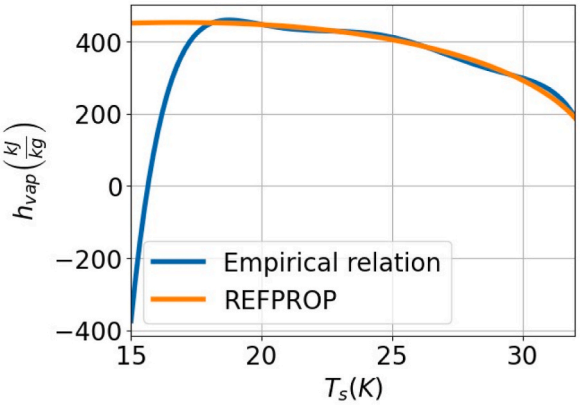

(e) Enthalpy of vaporisation versus saturated film temperature

Fig. 6. Cryogenic hydrogen properties computed by REFPROP versus empirical relations.

assess whether these correlations align with REFPROP output within the range of conditions relevant to this study.

Fig. 6a and b present empirical correlations for liquid temperature and density as functions of internal energy, both showing good agreement with REFPROP data. The correlation for liquid density as a function of internal energy is given in Eq. (7) [20]. Two correlations for liquid temperature as a function of internal energy are used, shown in Eq. (8) [20] and Eq. (9) [20], and are referred to as the 'First' and 'Second' correlations, respectively. Looking closely at Fig. 6a, it is observed that the second empirical relation is closer to REFPROP both at

lower temperatures (≈20 K) and higher temperatures (≈25 K) cryogenic LH_2. Therefore, Eq. (9) is preferred to Eq. (8).

$$\rho_l = -5.12074746\cdot10^{-7}\left(\frac{u_l}{1000}\right)^3 - 1.56628367\cdot10^{-5}\left(\frac{u_l}{1000}\right)^2 - 1.18436797\cdot10^{-1}\left(\frac{u_l}{1000}\right) + 7.06218354\cdot10^{1} \tag{7}$$

$$T_l = 1.44867559\cdot10^{-7}\left(\frac{u_l}{1000}\right)^3 - 2.53438808\cdot10^{-4}\left(\frac{u_l}{1000}\right)^2 + 1.05449468\cdot10^{-1}\left(\frac{u_l}{1000}\right) + 2.03423757\cdot10^{1} \tag{8}$$

$$T_l = -0.0002041552\left(\frac{u_l}{1000}\right)^2 + 0.1010598604\left(\frac{u_l}{1000}\right) + 20.3899281428 \tag{9}$$

Fig. 6c shows the correlation for the saturated vapour temperature as a function of pressure, as shown in Eq. (10) [20], where $F_{PSI\to Pa} = 6894.75729$. Although in general a good similarity is observed, around 10 bar the difference between the relation and REFPROP suddenly increases. Since 10 bar is significantly higher than the expected operating pressure, the correlation is considered suitable for the application in the model.

$$T_v = 0.1 + \left(-1.603941638811\cdot10^{-11}\left(\frac{P}{F_{PSI\to Pa}}\right)^6 + 7.830478134841\cdot10^{-9}\left(\frac{P}{F_{PSI\to Pa}}\right)^5 - 1.549372675881\cdot10^{-6}\left(\frac{P}{F_{PSI\to Pa}}\right)^4 + 1.614567978153\cdot10^{-4}\left(\frac{P}{F_{PSI\to Pa}}\right)^3 - 9.861776990784\cdot10^{-3}\left(\frac{P}{F_{PSI\to Pa}}\right)^2 + 4.314905904166\cdot10^{-1}\left(\frac{P}{F_{PSI\to Pa}}\right)^1 + 1.559843335080\cdot10^{1}\right) \tag{10}$$

The relation between saturated liquid density versus vapour temperature is visualised in Fig. 6d, for which the empirical relation is displayed in Eq. (11) [20]. Overall, a good resemblance is observed between REFPROP and the correlation, however, below 16 K a discrepancy can be observed. As this is lower than the expected operating temperature, this correlation is considered suitable for the model.

$$\rho_{l_{@T_v}} = -5.24588\cdot10^{-5}\cdot T_v^6 + 7.39502\cdot10^{-3}\cdot T_v^5 - 4.29976\cdot10^{-1}\cdot T_v^4 + 1.31922\cdot10^{1}\cdot T_v^3 - 2.25208\cdot10^{2}\cdot T_v^2 + 2.02705\cdot10^{3}\cdot T_v - 7.43508\cdot10^{3} \tag{11}$$

Fig. 6e shows the empirical relation, as shown in Eq. (12) [20], for the enthalpy of vaporisation. One can observe that around 18 K, a large discrepancy is observed between REFPROP and the correlation, which is very close to typical operation conditions. Consequently, this correlation is excluded from the model in favour of using REFPROP data directly.

$$\Delta h_v = 1000\cdot\left(-0.0024454517204 87T_s^6 + 0.3629946692976T_s^5 - 22.28028769483T_s^4 + 723.6541112107T_s^3 - 13116.31006512T_s^2 + 125780.2915522T_s - 498095.5392318\right) \tag{12}$$

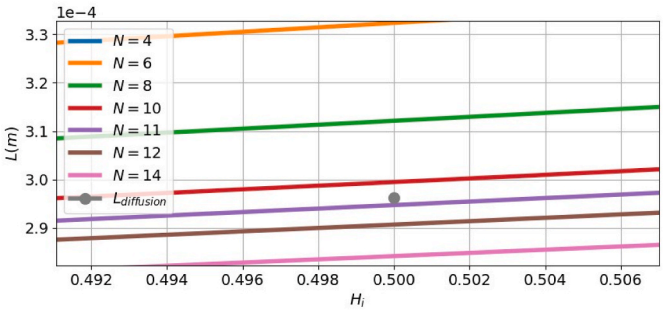

Fig. 7. Relation between the discretised length scales and the number of nodes.

3.2.4. Optimal number of nodes

To ensure accurate modelling of heat transfer near the saturated film, it is essential that the spatial resolution of the computational grid is sufficient to capture thermal gradients that occur across very short distances. As discussed in Section A.9, the characteristic length over which thermal diffusion occurs is known as the diffusion length, which is defined at the midpoint between the first and second grid points.

In previous work by Petitpas [20], the number of grid points in the vapour and liquid phases was arbitrarily set to 4 and 3, respectively, without verification of whether this resolution adequately resolved the diffusion length near the interface. This raises the question whether a higher number of nodes is needed to properly capture the heat transfer behaviour at the saturated film.

To address this, the discretised length scales from Fig. 27 are evaluated for different node counts and compared to the analytically calculated diffusion length at the midpoint between the first and second grid. The results, shown in Fig. 7, indicate that a node count of $N = 11$ provides the closest match to the diffusion length. This ensures that the thermal boundary layer is physically resolved, avoiding unnecessary computational cost. Furthermore, it is observed that the optimal number of nodes is the same for both the vapour and liquid phases.

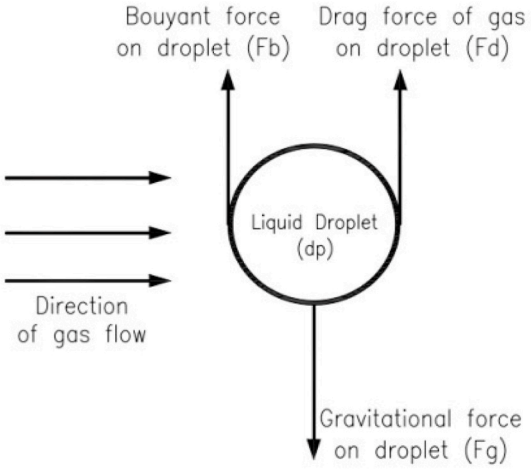

Fig. 8. Diagram showing the balance of forces acting on a water droplet in a horizontal steam line that is flowing under gravity [29].

3.2.5. Droplet model

To accurately simulate the experiment conducted by Hartwig et al. [22], in which LH_2 is injected into the ullage of a cryogenic tank using a spray bar, it is necessary to revise the tank model developed by Petitpas [20]. In this tank model, the top-fill injection process was represented in a highly simplified manner, assuming that only a small fraction of the injected LH_2 vaporises immediately upon entering the tank and contributes directly to the balances of the vapour phase. Although this assumption reduces model complexity, it neglects the physical interaction between the falling droplets and the surrounding cryogenic vapour. As a result, the droplet dynamics during top-fill operations is not accurately captured in the tank model.

To address this limitation, the current work integrates an established droplet model, originally developed by Wang and Ju [28] for LNG applications, into Petitpas' [20] tank model. This integration enables a more physically accurate representation of mass and energy exchange during top-spray filling by explicitly modelling the droplet dynamics, heat transfer, and phase change as the droplets fall through the ullage gas.

The following section provides a detailed overview of the droplet model and shows how it is embedded within the tank's mass and energy balances. The goal is not to introduce a new droplet model, but to improve the existing tank model by integrating a physically realistic spray-filling approach.

The force balance on the droplet, as shown in Fig. 8, is shown in Eq. (13). In order to determine the terminal velocity v_d, Eq. (13) is rewritten to Eq. (14). In this equation, the left term is gravity, while the first and second terms on the right side are, respectively, buoyancy force and drag force. The droplet diameter is denoted by D_d.

$$\rho_l g\left(\frac{\pi}{6}D_d^3\right) = \rho_v g\left(\frac{\pi}{6}D_d^3\right) + C_D\left(\frac{\pi}{4}D_d^2\right)\left(\rho_v\frac{v_d^2}{2}\right) \tag{13}$$

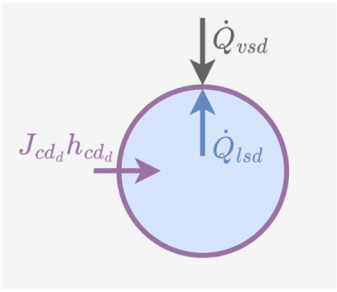

Fig. 9. Energy transfer in a single droplet.

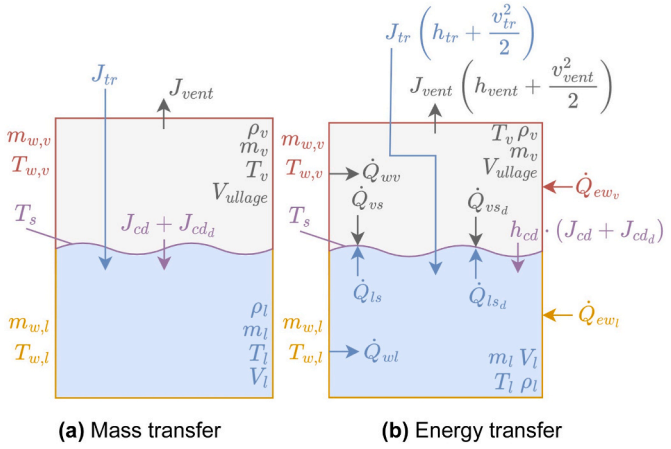

Fig. 10. Mass and energy transfer for the receiving tank including droplet model.

$$v_d = \sqrt{\frac{4gD_d(\rho_d - \rho_l)}{3C_D\rho_c}} \tag{14}$$

The droplet's time of fall is determined by Eq. (15).

$$t_d = \frac{D - h}{v_d} \tag{15}$$

The number of incoming droplets per unit time is calculated as Eq. (16). V_d is the volume of a single droplet. As the droplets are assumed to be perfect spheres, $V_d = \frac{1}{6}\pi D_d^3$.

$$\dot{N} = \frac{J_{tr}}{\rho_l V_d} \tag{16}$$

The Ranz-Marshall correlation is used to determine the amount of convective heat transfer between the vapour and the droplet freely falling [30], as shown in Eq. (17).

$$Nu = \frac{\alpha_d D_d}{k_v} = 2 + 0.6Re^{\frac{1}{2}}Pr^{\frac{1}{3}} \tag{17}$$

The energy transfer in a single droplet is shown in Fig. 9. It is assumed that the droplet-vapour interface is saturated at ullage

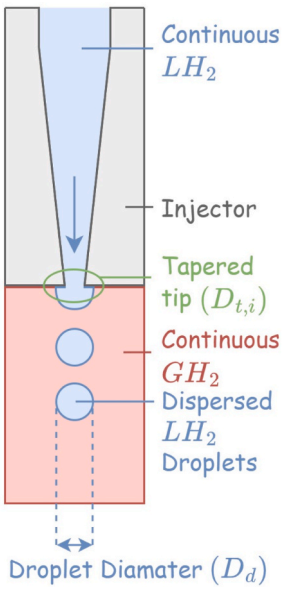

Fig. 11. Schematic showing the injection of LH_2 in the gaseous phase.

pressure. Therefore, the heat transfer from the vapour to the droplets is displayed in Eq. (18), where T_s is the saturated interface temperature and S_d is the surface area of a single droplet, which is for a sphere equal to $S_d = \pi D_d^2$.

$$\dot{Q}_{vsd} = [\alpha_d S_d (T_v - T_s) t_d] \dot{N} \tag{18}$$

Conduction inside a solid sphere subjected to an abrupt change in surface temperature is used to represent the heat transfer inside the liquid droplet [30] as shown in Eq. (19).

$$\dot{Q}_{lsd} = \left[1 - \frac{6}{\pi^2} e^{-\pi^2 Fo}\right] (\rho_l c_{p,l} V_d)(T_s - T_d)\dot{N} \tag{19}$$

T_d is the droplet temperature, which is considered equal to the bulk temperature of LH_2 at the end of the transfer line. *Fo* is the Fourier number, so that $Fo = \frac{4 a_l t_d}{D_d}$. a_l is the thermal diffusivity, which is equal to $a_l = \frac{\kappa}{\rho c_p}$. Given that energy is conserved at the droplet-vapour interface, the phase change mass flow on the droplet is expressed as Eq. (20), where positive values indicate condensation and negative values indicate evaporation.

$$J_{cd_d} = -\left(\frac{\dot{Q}_{lsd} + \dot{Q}_{vsd}}{h_{cd_d}}\right) \tag{20}$$

The mass and energy transfer for the receiving tank including droplet model is displayed in Fig. 10a and b respectively, which are adapted from Ref. [28].

Based on Fig. 10a, the mass transfer in the liquid and the vapour phase is derived in Eq. (21) and Eq. (22) respectively.

$$J_v = -J_{vent} - J_{cd} - J_{cd_d} \tag{21}$$

$$J_l = J_{tr} + J_{cd} + J_{cd_d} \tag{22}$$

Based on Fig. 10b, the heat transfer in the liquid and the vapour phase is derived in Eq. (23) and Eq. (24) respectively.

$$\dot{Q}_v = -J_{vent}\left(h_{vent} + v_{vent}^2\right) - h_{cd} \cdot \left(J_{cd} + J_{cd_d}\right) + \dot{Q}_{wv} - \dot{Q}_{vs} - \dot{Q}_{vs_d} - p\dot{dV} \tag{23}$$

$$\dot{Q}_l = J_{tr}\left(h_{tr} + v_{tr}^2\right) + h_{cd} \cdot \left(J_{cd} + J_{cd_d}\right) + \dot{Q}_{wl} - \dot{Q}_{ls} - \dot{Q}_{ls_d} + p\dot{dV} \tag{24}$$

A correlation for calculating the drag coefficient, C_D, in Eq. (14) is proposed by Brauer [31], which is shown in Eq. (25).

$$C_D = \frac{24}{Re} + \frac{3.72}{\sqrt{Re}} - \frac{4.83 \cdot 10^{-3}\sqrt{Re}}{1 + 3 \cdot 10^{-6} Re\sqrt{Re}} \tag{25}$$

The Re number of the LH_2 droplets when injected in the ullage of the tank can be calculated by Eq. (26) [32]. Here, $D_{t,i}$ is the diameter of the capillary tip, which is assumed to be $D_{t,i} = 0.8 D_d$.

A schematic of the LH_2 being injected into the ullage is displayed in Fig. 11

$$Re_d = \frac{\rho_d D_{t,i} v_d}{\mu_d} \tag{26}$$

By combining Eq. (14), Eq. (25), and Eq. (26), and applying the root-solver *fsolve* in Python, the drag coefficient can be determined. A drag coefficient of 0.47, which corresponds to a three-dimensional sphere in laminar flow at approximately $Re \approx 10^5$ [33], is used as an initial guess for the solver. Under typical operating conditions of 21 K, the resulting drag coefficient, Reynolds number, and terminal velocity are plotted as functions of droplet diameter in Fig. 12. It is observed that for droplet diameters smaller than 0.1 mm, the solver exhibits poor convergence behaviour.

Although these results offer valuable insights into the aerodynamic behaviour of droplets as a function of their diameter, it is equally important to consider the thermodynamic and operational implications of droplet sizing in the context of top spray filling. Smaller droplets have a larger specific surface area, which enhances the efficiency of vapour condensation and cooling during the fill process. However, reducing the droplet diameter also increases the flow resistance in the spray nozzle, requiring a higher pressure drop to maintain the same top fill rate [28].

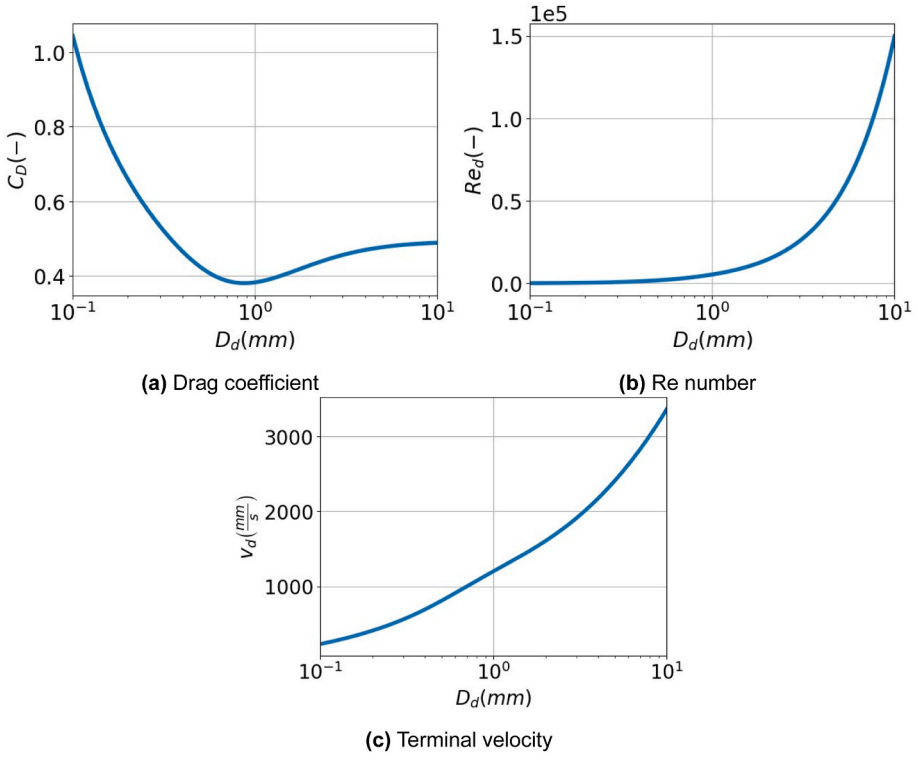

Fig. 12. Droplet properties versus diameter.

To balance these effects, a droplet diameter range of 0.4–8 mm is selected. Below 0.4 mm, the drag coefficient increases sharply, leading to significantly higher flow resistance; above 8 mm, the effectiveness of spray dispersion decreases. Therefore, this range is adopted as input for the sensitivity analysis described in Section 4.1.

3.2.6. Transfer line

As mentioned in Section 2.1, the effects of flashing, thermal mass, and imperfect insulation of the transfer line are not taken into account in the tank model. Therefore, the temperature of LH_2 at the end of the transfer line entering the receiving tank is equal to the temperature of LH_2 in the supply tank. However, as a simplified methodology to account for the decrease in pressure in the transfer line, it is assumed that the temperature at the end of the transfer line is equal to the LH_2 temperature in the receiving tank. Therefore, the fluid temperature on the transfer line is the average LH_2 in the supply and receiving tank, as shown in Eq. (27).

The properties of the fluid in the transfer line are assumed to be saturated at this LH_2 temperature. This assumption is considered valid, since the inlet saturation pressure during NVF in Fig. 4a is from $t = 200$ s significantly lower than the inlet pressure, implying that the liquid is subcooled and no two-phase flow is present in the transfer line. However, between the start of the NVF process at $t = 179$ s and $t = 200$ s, some two-phase flow might be present in the transfer line, which could cause discrepancies between the model and the experimental results.

$$T_{l_{tr}} = \frac{T_{l_{RT}} + T_{l_{ST}}}{2} \tag{27}$$

The tank is modelled such that, when the final fill level is reached, the supply valve closes and the leftover flow in the transfer line is transferred using the (same) pressure difference between the supply and receiving tank. However, in reality, the driving force due to the higher supply pressure vanishes as the supply valve closes. As a result, a pressure surge occurs in the pipe. Therefore, in reality, the supply valve requires time to close, thus showing a similar flow rate behaviour in the transfer line.

Therefore, this methodology is still implemented in the model. The refuelling process is assumed to be completed when the transfer line flow rate is less than $1{\cdot}10^{-3}\ \frac{kg}{s}$.

In addition, since no pump is specified to transfer the liquid from the supply tank to the receiving tank, it is assumed that the transfer is fed pressure, where the pressurised gas is GH_2. As mentioned in Section A.6, Petitpas' [20] tank model is simulating the pressure drop using a pressure feed system. Therefore, no modifications are required for modelling the feed system.

Next, the so-called transmission line delay constant is a model parameter used to model the transfer line state derivative. Although Petitpas' [20] tank model assumed a value of 10, it is of interest to find this constant based on the experimental results.

3.2.7. Specific heat and specific heat ratio

In Petitpas' [20] tank model, the specific heats and the specific heat ratio are considered constant. This is, however, modified using REFPROP so that those are determined by real equations of state.

3.2.8. Wall area

As said, a distinction is made in the temperature of the receiving wall that is in contact with the liquid and the vapour. Therefore, it is necessary to compute the corresponding wall areas. The area of the tank wall in contact with the liquid is calculated using Eq. (28) [34].

$$S_{wall,liquid} = 2\pi R h \tag{28}$$

Knowing that the surface area of a sphere $S_{sphere} = 4\pi R^2$, the area of the tank wall in contact with the ullage is calculated as $S_{wall,vapour} = S_{sphere} - S_{wall,liquid}$.

The average tank temperature is calculated using Eq. (29).

$$T_{wall,average} = \frac{S_{wall,vapour} T_{wall,vapour} + S_{wall,liquid} T_{wall,liquid}}{S_{sphere}} \tag{29}$$

3.2.9. Heat ingress

In the original tank model by Petitpas [20], heat ingress from the environment was treated as a fixed input, both for the liquid and the vapour in the supply tank and for the tank wall of the receiving tank. In this work, the transfer of environmental heat to the receiving tank wall is instead calculated explicitly, based on the conditions described in the experimental setup by Hartwig et al. [22].

The tank in the experiment was suspended within a vacuum chamber to minimise heat ingress into the tank. The vacuum chamber could achieve continuous vacuum levels up to $6.7{\cdot}10^{-3}$ Pa, which is considered a medium-high vacuum. As a result, heat ingress by means of conduction and convection is assumed to be negligible.

What remains is heat transfer by radiation. As no form of insulation to reduce radiation, such as MLI, is mentioned in Ref. [22] nor is visible in Fig. 3, it is assumed that radiation is the dominant mode of heat entry from the environment into the aluminium light weight tank. Heat transfer from radiation can be calculated by Eq. (30).

$$\dot{Q}_{rad} = \epsilon \sigma S \left(T_2^4 - T_1^4\right) \tag{30}$$

The emissivity for some material at cryogenic temperatures is obtained from Ref. [35]. The aluminium tank is assumed to be mechanically polished. In addition, the ambient temperature (T_2) is assumed to be 15 °C (or 288 K), while the tank wall temperature (T_1) was around 20 K. Therefore, it is assumed that the emissivity is equal to the emissivity of 290 K → 77 K plus the emissivity of 77 K → 4.2 K, so the emissivity is $\epsilon = 0.10 + 0.06 = 0.16$.

As mentioned in Section A.17, the tank wall is considered to be divided into two parts; one in contact with the liquid phase and one in contact with the vapour phase. Therefore, $\dot{Q}_{rad_v}$ is depending on the area and temperature of the tank wall in contact with the vapour, S_{wv} and T_{wv} respectively. The same holds for the liquid phase. The heat ingress into the supply tank is assumed 100 W, which would result in a heat flux of $q'' = 5.5\ \frac{W}{m^2}$.

3.2.10. Loss coefficient

The calculations for the steady flow through the transfer line are already presented in Section A.6, but are displayed here once more for clarity. Again, as shown in Eq. (31), the mass flow rate is dependent on energy losses during steady flow in the transfer line, indicated as α_{eff}.

$$J_{tr_0} = \alpha_{eff} \sqrt{\Delta p_{tot}} \tag{31}$$

The energy losses are calculated by Eq. (32) and can be divided into two categories as shown in Eq. (32), namely the major and minor energy losses.

$$\alpha_{eff} = \left(\alpha_v^{-2} + \alpha_{pipe}^{-2}\right)^{\frac{1}{2}} \tag{32}$$

The major losses are due to friction in the pipe, indicated by α_{pipe}, and are calculated according to Eq. (33), where μ_f is calculated in Section 3.2.2.

$$\alpha_{pipe} = 2\pi \left(\frac{D_{pipe}}{2}\right)^2 \sqrt{\frac{\rho_{tr}\left(\frac{D_{pipe}}{2}\right)}{\mu_f L_{pipe}}} \tag{33}$$

Minor losses are due to a variety of reasons, such as pipe fittings and bends, indicated by α_v and are calculated using Eq. (34). $\alpha_{\lambda tr}$ is the so-called loss coefficient, which is commonly called K. The loss coefficient is a constant that is directly proportional to the pressure drop across the component. As the K-factor increases, the resistance to flow through the component also increases.

Table 2
Additional input parameters.

Based on the experimental setup	Parameter	Value	Unit
described by Hartwig et al. [22]	V_{ST}	5.678	m^3
	V_{RT}	1.39	m^3
	$t_{w_{RT}}$	$1.39{\cdot}10^{-3}$	m
	R_{RT}	1.372	m
	m^2	40.37	kg
	D_{tr}	$2.54{\cdot}10^{-2}$	m
	$D_{\lambda_{tr}}$	$1.27{\cdot}10^{-2}$	m
	$S_{\lambda_{RT,vent}}$	$\left(\frac{2.21{\cdot}10^{-2}}{2}\right)^2 \pi$	m^2
Assumed	L_{tr}	20	cm
	ϵ_{tr}	1	μm
	T_{amb}	15	°C
	p_{amb}	1	ATM
	g	9.81	$\frac{m}{s^2}$

$$\alpha_v = \lambda_{tr} S_{\lambda_{tr}} \sqrt{\frac{2\rho_{tr}}{\alpha_{\lambda_{tr}}}} \tag{34}$$

Here $S_{\lambda tr}$ is calculated in Eq. (35).

$$S_{\lambda_{tr}} = 2\pi \left(\frac{D_{\lambda_{tr}}}{2}\right)^2 \tag{35}$$

In the experimental set-up, some pipe fittings and valve can be observed. However, it is unclear what exact pipe fittings are present in the system, which makes it difficult to compute the total loss coefficient. Petitpas [20] considered a loss coefficient of $K = 4$ in the model for a transfer line diameter of 2 inch or 50.8 mm, which is $\frac{50.8\ \text{mm}}{30\ \text{mm}} = 1.7$ times greater than the diameter considered of 30 mm. However, most of the fittings and valves showed a negative logarithmic trend between the diameter of the component and the corresponding loss coefficient. As a conservative approach, a linear increase is considered, which results in a loss coefficient of $K = 6.8$. However, because of the logarithmic trend, the loss coefficient obtained from the experiment is predicted to be higher.

Table 3
Relevant parameters and values for the sensitivity analysis of the model modification and validation.

Parameter	Symbol	Unit	Value
Loss coefficient	K	(−)	9 10 11 12 13
Droplet diameter	D_d	mm	0.4 1 2 4 6 8
Tip capillary-to-droplet diameter ratio	$\frac{D_{t,i}}{D_d}$	(−)	0.8 0.4
Transfer line length	L_{tr}	cm	20 200
Heat ingress by radiation	$\dot{Q}_{rad}$	%	50 100 150
Transfer line roughness	ϵ_{tr}	μm	1 10
Transmission line delay constant	τ_{tr}	(−)	3 5 7
Vent-opening pressure	$p_{RT,\lambda_{vent}1\to0}$	bar	1.1 2 2.5 3 3.18

3.3. Additional model input parameters

As noted in Section 2.2, Test 4 from the experiment by Hartwig et al. [22] is identified as the most reliable implementation of the rapid vented chill-and-fill method. The initial, boundary and final conditions for this test, used as input for the numerical simulation, are listed in Table 1. These values are taken directly from the experimental test matrix and correspond to the beginning and end of the no-vent fill (NVF) phase. As discussed in Section 2.2.1, it is observed that the maximum pressure in the RT is 3.345 bar, which decreases afterwards to 3.18 bar, after which some oscillating behaviour is noticed. Based on this, the venting valve is modelled such that it opened after the RT pressure increases above 3.345 bar and closes again when the pressure decreases to 3.18 bar. However, this is not in line with the information provided in the experiment, which described that the vent valve closed when pressure was reduced below 1.1 bar [22]. Some of the required model input parameters are directly available from the experimental data of Test 4, while others are not explicitly reported. For the latter, reasonable assumptions have been made. An overview of all additional input parameters used in the numerical model is provided in Table 2.

3.4. Simulation of the refuelling process for the experimental setup

Using the results from the sensitivity analysis, the Petitpas' [20]

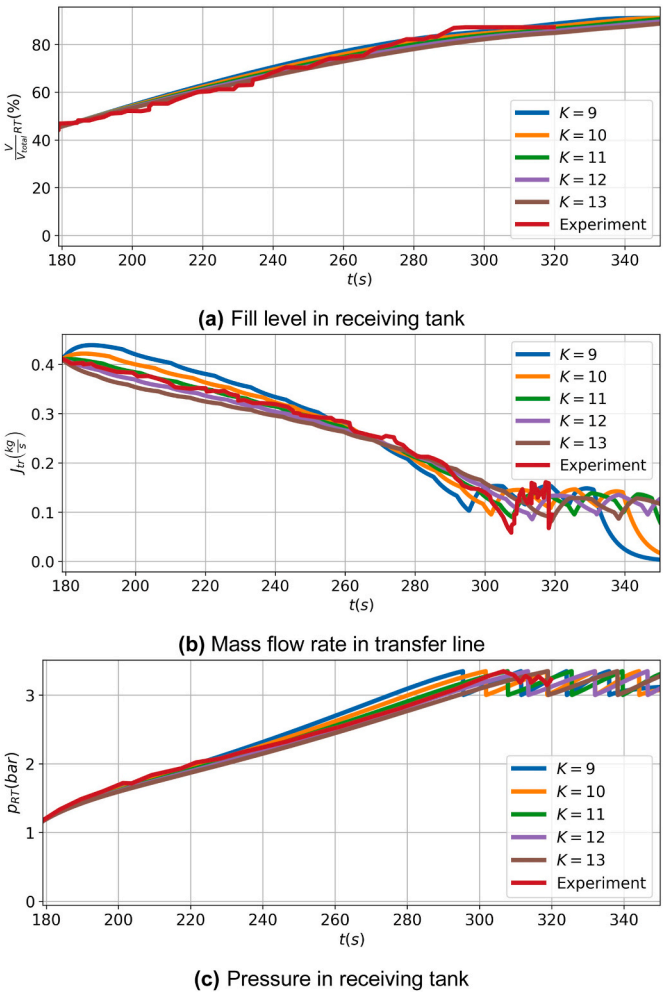

Fig. 13. Loss coefficient.

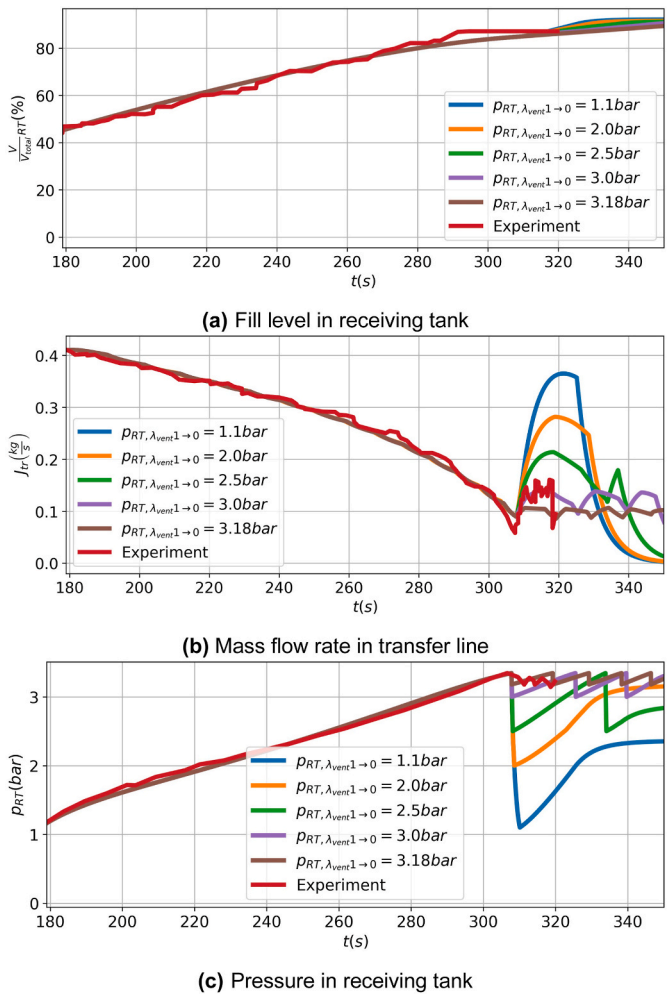

Fig. 14. Vent-closing pressure in receiving tank.

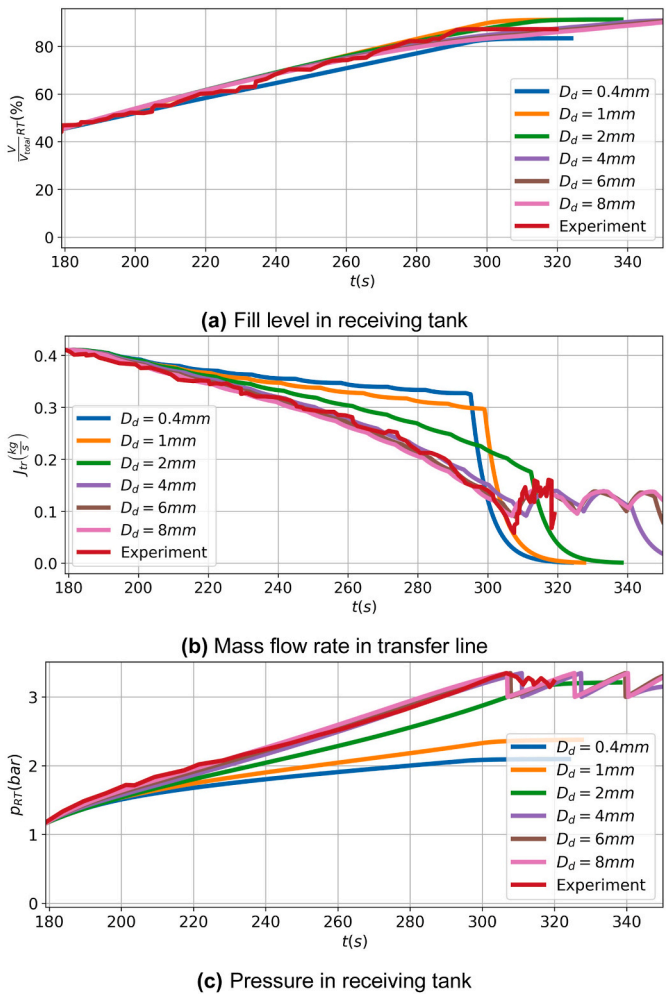

Fig. 15. Droplet diameter.

model is validated against the experimental data by Hartwig et al. [22], and the experimental data at the end of the NVF is compared with the model data. A complete list of model inputs used for the model modification and validation is provided in Table 6.

The simulations are performed using Spyder IDE 5.1.5 using conda Python 3.9.7 and REFPROP DLL version 10.0, on a laptop PC running on 64-bit Windows 10 Enterprise (2023), with an 12th Gen Intel(R) Core (TM) i5-1245U @1.60 GHz and a 16.0 GB DDR4 RAM.

4. Results

The results of the modification and validation of the model are provided in this section. First, the results of the sensitivity analysis are displayed in Section 4.1. Second, the results of simulating the experimental setup using Petitpas' [20] modified tank model are shown in Section 4.2.

4.1. Sensitivity analysis

A sensitivity analysis is performed to identify the model parameters that best align with the experimental results of Test 4 by Hartwig et al. [22]. The parameters considered and the values for which the sensitivity is examined are listed in Table 3. The sensitivity of those values on the transfer line mass flow rate, receiver tank pressure and fill level is analysed, as those are displayed in Fig. 4 during the NVF process and are also output parameters of Petitpas' [20] modified tank model. The results are summarised in this section. The label 'Experiment' in the figures refers to the experimental data from Test 4 reported by Hartwig et al. [22], against which the numerical results are compared.

4.1.1. Loss coefficient

In Fig. 13, one could observe that the loss coefficient significantly affects the transfer line mass flow rate, for which a lower loss coefficient resulted in a higher mass flow rate in the initial state of the NVF. In addition, the pressure in the RT is affected by modifying the loss coefficient, which is expected as the transfer line mass flow rate and RT pressure are related by the pressure drop. However, the fill fraction is not noticeably influenced. A loss coefficient of 11 is considered to match best the experimental data, which is significantly higher than the predicted value of 6.8 in Section 3.2.10. However, it is already argued that a higher loss coefficient is expected due to the logarithmic trend.

4.1.2. Vent-closing pressure in receiving tank

The vent-closing pressure in the RT showed to have a very significant impact on both the transfer line mass flow rate and the pressure in the RT, and to a lesser extent also on the fill fraction, as shown in Fig. 14. Although a vent-closing pressure of 3.18 bar matched best with the experimental data for the RT pressure, this value implied significant discrepancies with the experimental results for the transfer line flow rate. When considering the mass flow rate, a vent-closing pressure of 3 bar resulted in the best match to the experimental data. In addition, a vent-closing pressure of 1.1 bar, as mentioned in the experimental setup [22], resulted in even greater discrepancies for both the transfer line flow rate and the pressure in the RT. However, it is considered that a

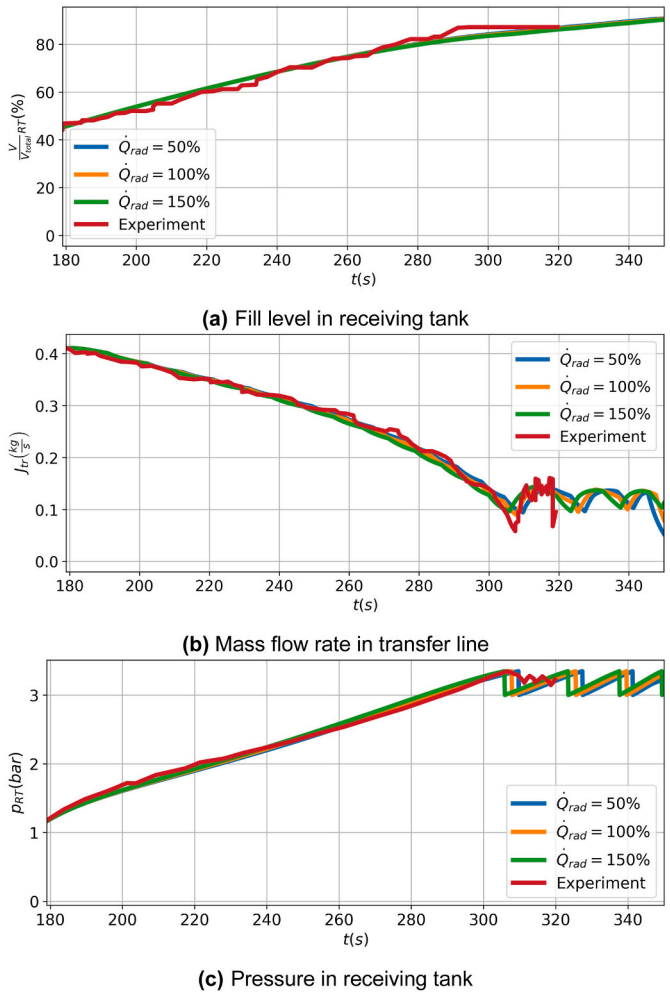

Fig. 16. Percentage of heat ingress by radiation.

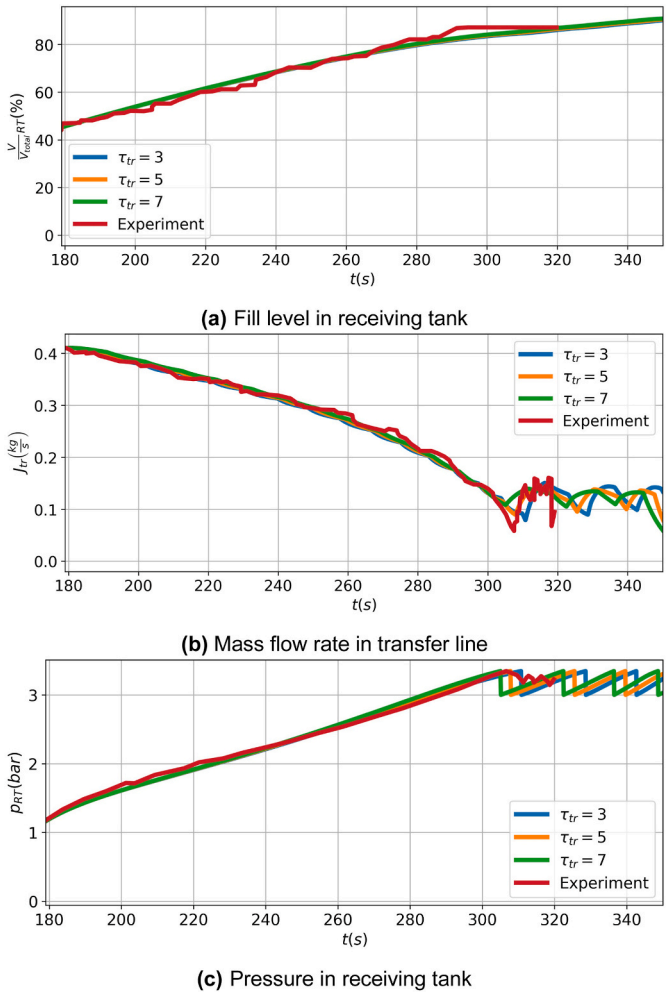

Fig. 17. Transmission line delay constant.

vent-closing pressure of 3 bar showed the best overall results with the experimental data.

4.1.3. Droplet diameter

As shown in Fig. 15, significant discrepancies can be observed with the experimental data for the mass flow rate of the transfer line and the RT pressure. The largest discrepancies are observed for a droplet diameter of $\leq$4 mm. The results for a droplet diameter of 6 mm and 8 mm are quite similar, but those of 6 mm are found to provide slightly better results with respect to the experimental data.

4.1.4. Heat ingress by radiation

Modifying the assumed heat ingress by radiation by $\pm$50 % showed some variation in the results for the pressure in the RT and the transfer line mass flow rate towards to end of the process, as displayed in Fig. 16. The assumed heat ingress is however providing the best matching results and so it is considered that no modifications are required.

4.1.5. Transfer line delay constant

The delay constant of the transfer line was shown to influence the mass flow rate in the transfer line and the pressure in the RT, mostly towards the end of the process, as seen in Fig. 17. It is observed that a value of 5 provided the best results compared to the experimental results, which is 50 % lower than the value of 10 considered in Petitpas' [20] tank model.

Table 4
Sensitivity analysis results for selected parameters.

Parameter	Symbol	Unit	Value
Loss coefficient	K	(–)	11
Droplet diameter	D_d	mm	6
Tip capillary-to-droplet diameter ratio	$\frac{D_{t,i}}{D_d}$	(–)	0.8
Transfer line length	L_{tr}	cm	20
Heat ingress by radiation	$\dot{Q}_{rad}$	%	100
Transfer line roughness	ϵ_{tr}	μm	1
Transmission line delay constant	τ_{tr}	(–)	5
Vent-opening pressure	$p_{RT,\lambda_{veni}1\to0}$	bar	3

4.1.6. Other parameters

The sensitivity analyses for the remaining parameters, including the tip capillary-to-droplet diameter ratio, the transfer line length, and the transfer line roughness, did not result in significant differences in the simulation outcomes; therefore, no figures are presented for these cases. As a result, the default assumptions of a tip capillary-to-droplet diameter ratio of 0.8, a transfer line length of 20 cm, and a surface roughness of 1 μm are considered appropriate.

4.1.7. Summary of sensitivity analysis results

A summary of the results of the sensitivity analysis is presented in Table 4, and the corresponding parameter values will be used to simulate the refuelling process for the experimental setup in Section 4.2.

Table 5
Comparison between experimental and numerical data at the end of the NVF process.

	t (s)	p_{RT} (bar)	$T_{RT,v}$ (K)	$m_{RT,v}$ (kg)	$T_{RT,l}$ (K)	$m_{RT,l}$ (kg)	$\left(\frac{V}{V_{total}}\right)_{RT}$ (%)	$T_{w,RT,avg}$ (K)
Experimental results [22]	338	1.4569	21.48	0.12	21.84	87.75	91	24.6
Model results	372	3.1203	25.84	0.44	21.51	87.63	91	22.7

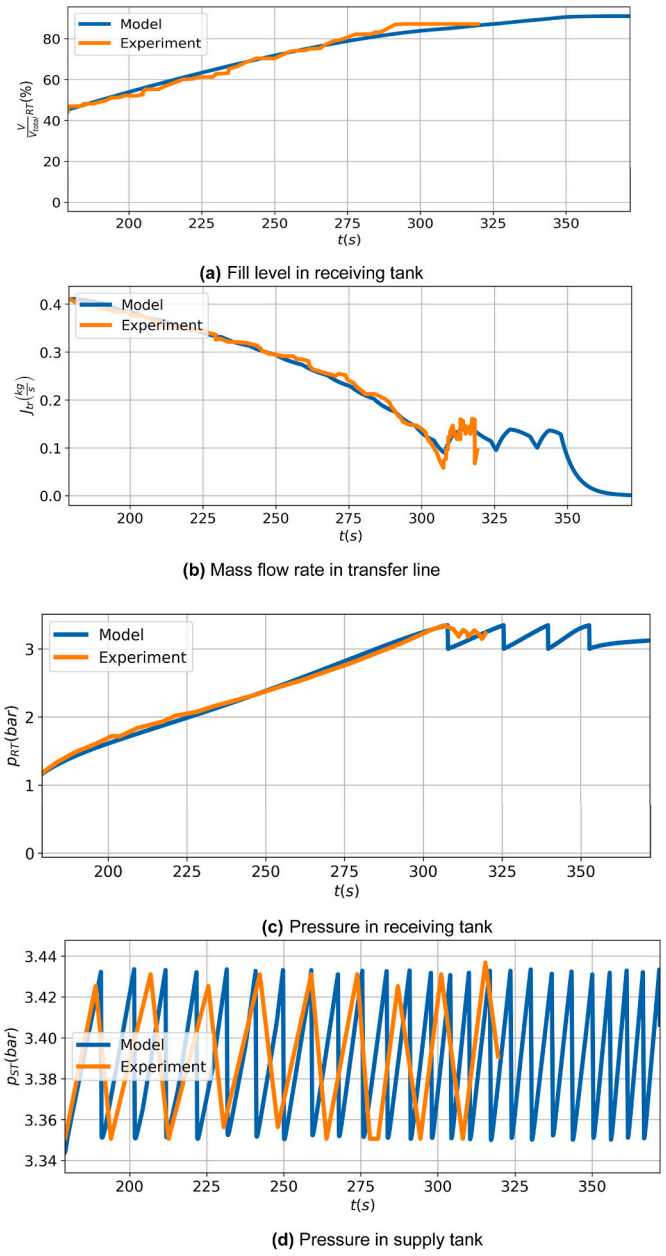

Fig. 18. Results of model modification and validation.

4.2. Simulating the refuelling process for the experimental set-up

The computational time is 12 min and 33 s using the hardware as specified in Section 3.4. A comparison between the experimental data from Test 4 by Hartwig et al. [22] and the numerical results of the tank model at the end of the no-vent filling (NVF) process is presented in Table 5. Large discrepancies can be observed between the results of the experiment and the model. Those discrepancies are expected to originate from the opening of the venting valve in the RT that are not expected for a non-vent fill, as explained in Section 2.2.1. The graphs showing the transient behaviour in the refuelling system are shown in Fig. 18.

First, the final refuelling time is 34 s longer for the model. As mentioned in Section 3.2.6, it is assumed that the refuelling process is completed when the mass flow rate of the transfer line is less than $1 \cdot 10^{-3}$ $\frac{kg}{s}$ to account for the time it takes to close the valve of the supply tank. In the model, the supply tank valve closes at $t = 348$ s and so 24 s are modelled to be required to close the supply tank valve. Therefore, in reality, the time required to close the valve is considered much shorter. However, even considering that the valve supply tank valve would close immediately, a discrepancy in fuelling time of 10 s is observed, implying a percentage difference of 6.1 %.

When comparing the results of the experiment and the model, it is found that the temperature and mass of the liquid have a 1.52 % and 0.14 % percentage difference, which are considered reasonably low.

However, comparing the vapour pressure, temperature and mass, larger percentage errors are observed, namely 72.3 %, 18.4 % and 114.3 % respectively. The pressure, vapour temperature, and vapour mass in the model at the end of the NVF are namely found to be significantly higher than in the experiment. However, the transient behaviour between the model and the experiment is considered rather similar until $t = 307$ s, as shown in Fig. 18c.

A vent-closing pressure of 3 bar is considered to show the best match with experimental data, however, this vent-closing pressure would not allow the pressure in the RT to be 1.4569 bar at the end of the experiment. Since temperature and pressure are dependent variables, a reduction in pressure also results in a reduction in vapour temperature. As the experimental data between $t = 320$ s and the end of the experiment are not provided, it is difficult to explain the behaviour of the RT vent valve during this time interval and therefore why the pressure (and therefore the temperature of the vapour) is so significantly reduced during this time interval. In addition, reducing the RT pressure would imply more venting and, therefore, a lower vapour mass in the tank.

In addition, the model considers the vapour temperature in the top node of the tank. The experiment determines the vapour temperature using a sensor at 91.5 % of the tank level [22], which is not at the top of the tank. As the highest GH_2 temperatures are obtained at the top of the tank, some temperature differences are expected to originate from this offset in sensor location.

Next, a percentage error of 8.0 % is observed between the mass averaged RT wall temperature when comparing the model and the experiment. As shown in Eq. 3.2.8, the averaged RT wall temperature is calculated using the area of the tank wall in contact with the vapour and liquid and their corresponding wall temperatures. However, the experiment by Hartwig et al. [22] also takes into account the mass and temperature of the lid. Although the thickness of the lid is unknown, it is considered that the lid makes a significant contribution to the total mass. As the lid is in contact with the top part of the tank and therefore with the GH_2 with the highest temperature, it is assumed that the combination of significant mass and high temperature causes the lid to increase the RT wall temperature averaged by mass in the experiment compared to the model.

Finally, as shown in Fig. 18d, the venting frequency of the model is significantly higher than in the experiment. This is expected to originate

from two major aspects, which both involve the vaporiser.

The first aspect is the vaporiser valve flow coefficient, which determines the flow into the vaporiser; a higher valve flow coefficient results in a higher mass flow rate entering the vaporiser. As a result, the pressure in the supply tank is increased faster, and so a higher venting frequency is observed. Based on the results, reducing the valve flow coefficient of the vaporiser would result in a better venting behaviour in the supply tank according to the experiment.

The second aspect is the initial condition of the vaporiser. An attempt is made to give some non-zero initial conditions to the vaporiser, but as the focus of the model modification and validation is rather on the receiving tank than on the supply tank, those input parameters are not in detail optimised.

5. Discussion and conclusions

Recently, Mangold et al. [10] analysed the LH_2 refuelling system and concluded that the procedure did not negatively impact aircraft turn-around times. They established a refuelling rate of 20 $\frac{kg}{s}$ based on the assumption that energy flow rates should match those of kerosene-powered aircraft, thereby ensuring similar turnaround times. However, this assumption contradicted the findings of Clean Hydrogen Joint Undertaking, who reported that LH_2 refuelling times are 1–3 times longer than those for kerosene, depending on the range of the aircraft.

The primary focus of this study is to simulate the LH_2 refuelling process through detailed numerical modelling to gain insight into the thermal phenomena involved. Petitpas' [20] tank model served as the foundation for these simulations; however, it had not previously been validated against experimental data. With the recent availability of experimental results from Hartwig et al. [22], it is possible to directly compare simulation outcomes with appropriate experimental test data.

Petitpas' [20] original tank model cannot accurately reproduce the refuelling behaviour observed in the experiments without significant modification. Most importantly, the inclusion of a droplet spray model proved essential to realistically capture the top-fill injection method used in the experimental setup.

Without this addition, the simulation results deviated substantially from the experiment. Moreover, several model parameters had been assumed without clear justification. To address this, a sensitivity analysis is performed to assess the impact of these assumptions on key outputs such as tank pressure, fill level, and mass flow rate. Further improvements included replacing the original heat transfer correlations with more appropriate formulations from the established literature. The sensitivity analysis highlighted that the loss coefficient and vent-closing pressure had the most significant impacts on the model's output. A lower loss coefficient resulted in higher mass flow rates and affected the receiver tank pressure due to the pressure drop relationship. A vent-closing pressure of 3 bar is found to be the best overall match of the experimental data, although it resulted in some discrepancies with the flow rate of the transfer line.

Other parameters, such as droplet diameter, transfer line delay constant, and heat ingress by radiation, had notable effects, but varied in significance. Specifically, the change in droplet diameter affected the mass flow rate of the transfer line and the pressure of the receiver tank, with a diameter of 6 mm providing the closest match to the experimental data. However, it could be argued that the diameter of the droplets obtained is relatively large, since the literature typically reports LH_2 droplet sizes on the order of magnitude of 0.15 mm [36,37]. The delay constant of the transfer line influenced the mass flow rate and the pressure of the receiver tank towards the end of the process, with a value of 5 being the most accurate. In contrast, parameters such as the length and roughness of the transfer line had a minimal impact on the results.

Although some discrepancies are observed towards the end of the refuelling process, the model's transient behaviour is consistent with the experimental data for the majority of the process. These discrepancies may be attributed to factors not fully captured by the model or uncertainties in the experimental setup.

In conclusion, the modified tank model has shown its effectiveness in simulating the LH_2 refuelling process. Sensitivity analysis provided valuable insight into the impact of various parameters, leading to improved model accuracy. Despite some remaining discrepancies, the model effectively captures the essential dynamics of the LH_2 refuelling process and serves as a useful tool for further analysis and optimisation in the field.

CRediT authorship contribution statement

L. ten Damme: Writing – original draft, Validation, Formal analysis. **M. van Put:** Writing – review & editing, Supervision, Resources, Project administration. **A. Gangoli Rao:** Writing – review & editing, Validation, Supervision, Investigation, Conceptualization, Visualization, Writing – original draft.

Declaration of competing interest

The authors declare that they have no known competing financial interests or personal relationships that could have appeared to influence the work reported in this paper.

Appendix

A. Detailed Explanation of Petitpas' Model

Each block of the model flow chart, as shown in Fig. 2, is discussed in detail in this appendix. The purpose of this appendix is to provide a comprehensive and transparent explanation of the methodology used, as well as to offer a detailed scientific foundation for each part of the tank model developed by Petitpas [20]. Although the implementation by Petitpas [20] resulted in a functional numerical model, it often lacked explicit references to the underlying scientific principles. Therefore, this appendix aims to clarify the model structure and to explain the rationale behind the equations used, by linking them to established physical laws and published scientific formulas. This helps ensure the model can be properly understood, tested, and improved in future work.

A.1. The ODE Solver

The system of ODEs was considered stiff, implying that certain numerical methods involved are numerically unstable, and so small steps must be taken to obtain satisfactory results. The considered solver was MATLAB's *ode15s* solver, for which the detailed working principle is outside the scope of this study, but an in-depth analysis can be found in Ref. [38].

The initial value problem that must be solved was derived from Ref. [39] and is shown in Eq. (36).

$$\begin{aligned} &\frac{d\mathbf{x}}{dt} = f(t, \mathbf{x}) \\ &t = \left[t_0, t_{final}\right] \\ &\mathbf{x}(t_0) = \mathbf{x}_0 \end{aligned} \tag{36}$$

The goal is to obtain $\mathbf{x}$ for $t_0 < t \leq t_{final}$ by solving the initial value problem.

As mentioned earlier, the green block in Fig. 2 indicates that when the vent valve of the ET changes state (open ↔ closed), the ODE solver stops. This is required as the state of the ET vent valve influences the mass and energy balance in the ET. The *ode15s* incorporates a function to detect when certain events occur during the solution of an ODE and then stops the solution. Considering that the ET vent valve changes state at (t+1), the ODE solver stops at t and $\mathbf{x}$ is obtained for [t_0,t]. However, as one wants to solve $\mathbf{x}$ for [t_0,t_{final}], $\mathbf{x}$ must yet be solved for (t,t_{final}]. Therefore, the ODE solver is again executed with a changed ET vent state, however now the initial condition is taken at t, such that $\mathbf{x}_0 = \mathbf{x}(t)$. This process is repeated until $\mathbf{x}$ is obtained for [t_0,t_{final}].

A.2. Computation of x_0

The blue block is used to obtain the initial state variables. The components of the initial state variables are displayed in Eq. (37).

$$\begin{aligned} \mathbf{x}_0 = \Big[&m_{l_{ST_0}}, \mathbf{u}_{l_{ST_0}}, m_{v_{ST_0}}, \mathbf{u}_{v_{ST_0}}, T_{s_{ST_0}}, J_{tr_0}, m_{vap_0}, \\ &J_{boil_0}, m_{l_{ET_0}}, \mathbf{u}_{l_{ET_0}}, m_{v_{ET_0}}, \mathbf{u}_{v_{ET_0}}, T_{s_{ET_0}}, T_{w_{ET_0}} \Big] \end{aligned} \tag{37}$$

The input variables are shown in Fig. 19. For some parameters, such as the critical pressure and temperature of parahydrogen, the values were provided because these were considered generic. In addition, equations are provided to show how some initial parameters are dependent on others. The starting time of the integration interval was set to 0s, and the final time was set to t_{final}.

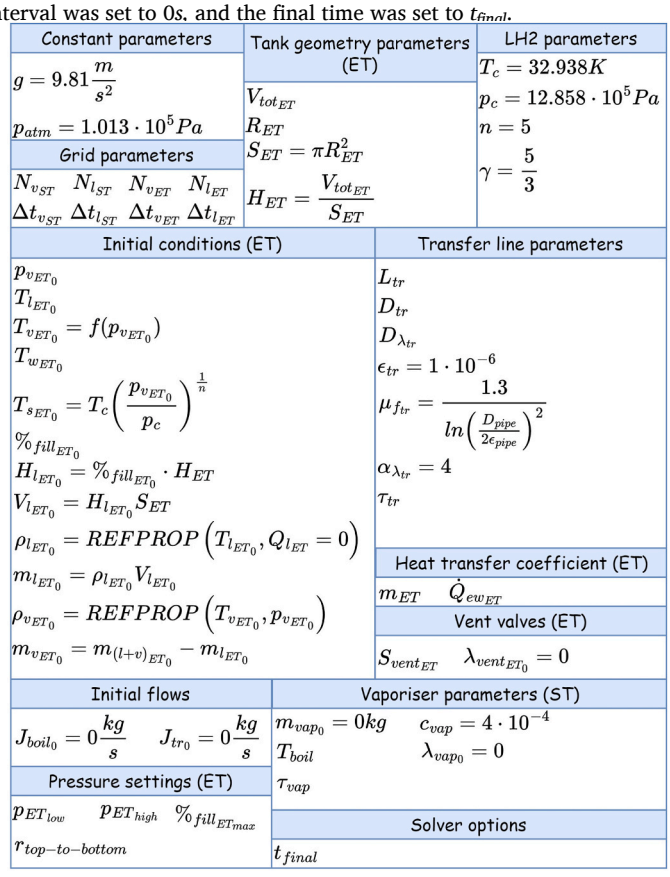

Fig. 19. Input variables

A.3. State Derivatives

The yellow blocks are used to obtain the state derivatives. This part of the model is most extensive and complex, which makes it rather difficult to discuss in a concise manner. Each yellow block as shown in Fig. 2 is discussed in this section, for which some blocks cover only a few lines of code and are rather straightforward, while others cover much larger parts of code. As the dynamic behaviour in the ET was of the most interest and because of the similarity between the ET and ST, most of the equations were only derived for the ET.

A.4. Initialisation of calculations

Next, the initial calculations for ET are performed in Fig. 20. In the following, it is discussed what happens in every step in the ET.

1. First, the initial state variables are obtained simply by considering that $\mathbf{x} = \mathbf{x}_0$.

2. The bulk liquid density is calculated as a function of its internal energy in the bottom node, which was provided in REFPROP based on the work of Younglove (1982) [40]. Now, the tanks and ullage volumes can be calculated as well as the density of the vapour.
3. The vapour temperature and quality are calculated by REFPROP on the basis of the vapour density and internal energy in the top nodes. As REFPROP cannot handle two-phase flow, if $0 \leq Q \leq 1$, then REFPROP calculates the vapour pressure based on the saturated vapour temperature. The amount of liquid in the two-phase flow is calculated and added to the bulk liquid volume. To do so, the density of a saturated liquid at the temperature of the vapour was computed using a correlation. When $Q > 1$ the vapour pressure is again calculated by REFPROP based on the vapour density and the internal energy at the top node of the tank. For the ET, the height of the bulk liquid is now calculated. Finally, the pressure of the bulk liquid is computed so that the total pressure can be determined.
4. The liquid is assumed to be in its saturated state. The temperature in each node of the liquid is calculated using a correlation, as there is no direct relation for the saturated liquid temperature as a function of internal energy in REFPROP. The temperature in the vapour nodes is determined by REFPROP based on the pressure and the internal energy in each node, with the exception of the top, as this one was already calculated, where the internal energy was divided by a factor of 1.5. However, this was considered a mistake and was therefore not used.
5. The interface area between the liquid and the vapour for the ET is simply the cross-sectional area.

Initial calculations (ET)

$$\rho_{l_{ET}} = f\left(u_{l_{ET}}(N_{l_{ET}})\right) \quad (1)$$

$$V_{l_{ET}} = \frac{m_{l_{ET_0}}}{\rho_{l_{ET}}}$$

$$V_{ullage_{ET}} = V_{tot_{ET}} - V_{l_{ET}}$$

$$\rho_{v_{ET}} = \frac{m_{v_{ET}}}{V_{ullage_{ET}}}$$

$$T_{v_{ET}}(N_{v_{ET}}) = REFPROP\left(\rho_{v_{ET}}, u_{v_{ET}}(N_{v_{ET}})\right) \quad (2)$$

$$Q_{ET} = REFPROP\left(\rho_{v_{ET}}, u_{v_{ET}}(N_{l_{ET}})\right)$$

$$0 \leq Q_{ET} \leq 1$$

$$p_{v_{ET}} = REFPROP(T_{v_{ET}}, Q_{ET} = 1)$$

$$\rho_{l_{ET_{@T_{v_{ET}}}}} = f\left(T_{v_{ET}}(N_{v_{ET}})\right)$$

$$H_{l_{ET}} = V_{l_{ET}} + \frac{(1 - Q_{ET}) m_{v_{ET}}}{\rho_{l_{ET_{f(T_{v_{ET}})}}} S_{ET}}$$

$$Q_{ET} > 1$$

$$p_{v_{ET}} = REFPROP\left(\rho_{v_{ET}}, u_{v_{ET}}(N_{v_{ET}})\right)$$

$$H_{l_{ET}} = \frac{V_{l_{ET}}}{S_{ET}}$$

$$p_{l_{ET}} = \rho_{l_{ET}} \cdot g \cdot H_{l_{ET}}$$

$$p_{tot_{ET}} = p_{v_{ET}} + p_{l_{ET}}$$

$$T_{l_{ET}}(i) = f\left(u_{l_{ET}}(i)\right) : i \in \{1, 2, \ldots, N_{l_{ET}}\} \quad (3)$$

$$T_{v_{ET}}(i) = REFPROP\left(p_{v_{ET}}, u_{v_{ET}}(i)\right) : i \in \{1, 2, \ldots, N_{v_{ET}} - 1\}$$

$$S_{l,v-interface_{ET}} = S_{ET_{bottom}} \quad (4)$$

Fig. 20. Initial calculations (ET)

A.5. Surface Temperature (ET)

Now, the state derivatives for the saturated film temperature in the ET is computed, as well as the state derivative for the mass flow rate through the transfer line. The equations are displayed in Fig. 21. The temperatures of the saturated film of ET is computed by equation (8) of [18], followed by computing the corresponding state derivatives.

Surface temperature (ET)

$$T_{s_{ET_0}} = T_c \cdot \left(\frac{p_{v_{ET}}}{p_c}\right)^{\frac{1}{n}}$$

$$\frac{dT_{s_{ET}}}{dt} = \frac{\left(T_{s_{ET_0}} - T_{s_{ET}}\right)}{\Delta t_{l_{ET}}}$$

Fig. 21. Surface temperature (ET)

A.6. Transfer Line

1. For slow fill, the transfer line chill down valve is open and the transfer line fill valve is closed, resulting in a $\lambda_{tr} = 0.5$, while for (reduced) fast fill, both valves are open, resulting in $\lambda_{tr} = 1$. Then, the state of the vaporiser valve was calculated as a function of the vapour pressure in the ST and the set pressure in the ST to meet the fill requirements, as shown in Equation (A11) of [18]. Also, the vent valve in ST might open if the vapour pressure

in the ST becomes too high, and so is a function of the vapour pressure in the ST and the set pressure in the ST, as indicated in equation (A12) of [18]. The temperature in the transfer line was considered to be equal to the temperature in the bottom node of the ST. The corresponding density was calculated using REFPROP at this temperature for a quality of zero.

2. The steady mass flow rate in the transfer line was calculated using equation (40) of [18]. The pressure drop between ST and ET is based on a gas pressure input system where the pressurised gas is GH_2. The mass flow rate through the transfer line is influenced by the friction in the line, which is composed of the friction in the pipe and valve, as shown in equation (41) of [18]. The friction in the pipe is calculated according to equation (35) of [18]. The friction in the valve is calculated according to equation (34) of [18].
3. Finally, the state derivative for the mass flow rate was based on equation (44) of [18].

Transfer line

1

$$\lambda_{tr} = 0.5/1$$
$$\lambda_{vap} = f(p_{v_{ST}}, p_{fill_{ST}})$$
$$\lambda_{vent_{ST}} = f(p_{v_{ST}}, p_{fill_{ST}})$$
$$T_{tr} = T_{l_{ST}}\left(N_{l_{ST}}\right)$$
$$\rho_{tr} = REFPROP\left(T_{tr}, Q_{tr} = 0\right)$$

2

$$J_{tr_0} = \alpha_{eff}\sqrt{p_{tot_{ST}} - p_{tot_{ET}}}$$
$$\alpha_{eff} = \left(\alpha_v^{-2} + \alpha_{pipe}^{-2}\right)^{\frac{1}{2}}$$
$$\alpha_{pipe} = 2\pi\left(\frac{D_{pipe}}{2}\right)^2\sqrt{\frac{\rho_{tr}\left(\frac{D_{pipe}}{2}\right)}{\mu_f L_{pipe}}}$$
$$\mu_f = \frac{1.3}{ln\left(\frac{R_{tr}}{\epsilon_{tr}}\right)^2}$$
$$\alpha_v = \lambda_{tr} S_{\lambda_{tr}}\sqrt{\frac{2\rho_{tr}}{\alpha_{\lambda_{tr}}}}$$
$$S_{\lambda_{tr}} = 2\pi\left(\frac{D_{\lambda_{tr}}}{2}\right)^2$$

3

$$\frac{dJ_{tr}}{dt} = \frac{J_{tr_0} - J_{tr}}{\tau_{tr}}$$

Fig. 22. Transfer line

A.7. Vaporiser (ST)

Then, the state derivative for the vaporised mass and the boiling mass flow rates in the ST are calculated in Fig. 23, as shown in the following steps.

1. The mass flow rate through the vaporiser valve was derived in equation (22) of [18].
2. The state derivative for the vaporised mass is calculated in accordance with Equation (21) of [18].
3. In addition, the state derivative for the boiling mass flow rate is computed according to equation (21) of [18].

Vaporiser (ST)

1

$$J_{vap} = c_{vap}\lambda_{vap}\sqrt{2\rho_{l_{ST}}\left(p_{tot_{ST}} - p_{atm}\right)}$$

2

$$m_{vap} \leq 0$$
$$J_{boil_0} = 0 \qquad J_{boil} = max(0, J_{boil})$$
$$\frac{dm_{vap}}{dt} = max(0, J_{vap} - J_{boil})$$
$$m_{vap} > 0$$
$$J_{boil_0} = J_{vap}$$
$$\frac{dm_{vap}}{dt} = J_{vap} - J_{boil}$$

3

$$\frac{J_{boil}}{dt} = \frac{J_{boil_0} - J_{boil}}{\tau_{vap}}$$

Fig. 23. Vaporiser in ST

A.8. Vent Flow (ET)

Here, the mass flow rate for the ET vent line is calculated in Fig. 24 by considering whether the flow is choked or not [41]. It must be noted that this equation is based on flows through holes and not pipes.

Vent flow (ET)

$$J_{vent_{ET}} = \lambda_{vent_{ET}} f\left(S_{vent_{ET}}, \gamma, \rho_{v_{ET}}, p_{v_{ET}}, p_{atm}\right)$$

Fig. 24. Vent flow (ET)

A.9. Heat Transfer between the Saturated Film and Vapour and Liquid Phases (ET)

The heat transfer between the saturated film and the vapour and liquid phases is now calculated for ET in Fig. 27. The step-by-step approach is given below.

1. First, the quality of the flow is calculated by REFPROP based on the vapour density and the internal energy in the top node. If $0 \leq Q_{ET} \leq 1$, then PR_v, κ_v, μ_v, c_{vv}, c_{pv} and β_v are computed by REFPROP based on the vapour temperature in the top node and a quality of 1. If $Q_{ET} > 1$, then PR_v, κ_v, μ_v, c_{vv}, c_{pv} and β_v are computed by REFPROP based on the vapour pressure and the internal energy in the top node. PR_l, κ_l, μ_l, c_{vl}, c_{pl} and β_l are computed by REFPROP based on the liquid temperature in the bottom node and a quality of 0.
2. The grid size for the vapour phase for the ET was set to 3 and 4 respectively. The relation between the discretised length scales and the number of nodes is displayed in Fig. 26. For the ET, L_{vmin} is the diffusion length within the vapour, which determines length scale for the midpoint between the first and second grid. The diffusion length $L_d = \sqrt{Dt}$ and the thermal diffusion length $D = \frac{\kappa}{\rho c_p}$.
   Then, the distance between the saturated film and every other vapour node is computed, for which N_v is the top vapour node.
3. The grid size for the liquid phase for the ET was set to 3. Again, the relation between the discretised length scales and the number of nodes is displayed in Fig. 26. For the ET, L_{lmin} is the diffusion length within the liquid, which determines length scale for the midpoint between the first and second grid. The diffusion length $L_d = \sqrt{Dt}$ and the thermal diffusion length $D = \frac{\kappa}{\rho c_p}$. Then, the distance between the saturated film and every other liquid node is computed, for which N_l is the bottom liquid node.
4. By considering that $\dot{Q}_{cond} = \dot{Q}_{conv} = \alpha A \Delta T = \frac{\kappa A \Delta T}{\Delta x}$, the heat transfer coefficient due to conduction between the saturated film and the vapour/liquid can be determined as $\alpha = \frac{\kappa}{\Delta x}$, where Δx is the diffusion length which was determined to be $L\left(H_{\frac{1}{2}}\right)$. The convective heat transfer coefficient for the liquid and vapour is based on $Nu = 0.156(Ra)^{\frac{1}{3}}$. The Rayleigh number is calculated according to equation (A4) of [18].
5. For the ET, the net heat transfer between the vapour/liquid to the saturated film due to conduction is calculated by $\dot{Q}_{cond} = \dot{Q}_{gen} + \frac{dE}{dt}$. $\dot{Q}_{gen} = \alpha_{cond} S_{l,v-interface} \Delta T - \frac{de}{dt}$, where ΔT is the temperature difference between the first vapour node $L(H_0)$ and the saturated film. $\frac{dE}{dt}$ is the change in internal energy. For the net heat transfer between the vapour and the saturated film $\frac{dE}{dt} = L_v(H_0) c_{v_v} \rho_v \frac{dT_s}{dt}$. For the net heat transfer between the liquid and the saturated film,

   $\frac{dE}{dt} = L_l(H_0) c_{p_l} \rho_l \frac{dT_s}{dt}$. As one can observe, the current unit of $\frac{dE}{dt}$ is $\frac{W}{m^2}$. This is considered a mistake in the work of Petitpas, as it is evaluated that the interface area $S_{l,v-interface}$ must be included.

Again, for the ET, the heat transfer from the vapour to the saturated film due to convection is calculated according to equation (4) from Ref. [18], where H is the Heaviside step function. The heat transfer from the saturated film to the liquid due to convection is calculated according to equation (5) from Ref. [18], where again H is the Heaviside step function. The final heat transfer between the saturated film and both the vapour and liquid is calculated by equation (6) of [18], which is graphically displayed in Fig. 25. For example, if $T_s > T_l$, $\dot{Q}_{lconv} = 0$ (due to the Heaviside function), and the only possible mode of heat transfer in the liquid phase is conduction, as displayed in Fig. 25a and b.

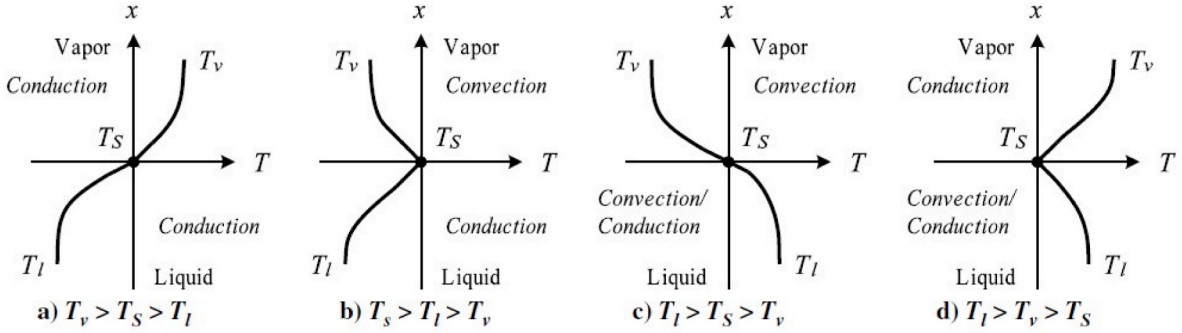

Fig. 25. Possible modes of heat transfer between the saturated film and the liquid and vapour phases [18]

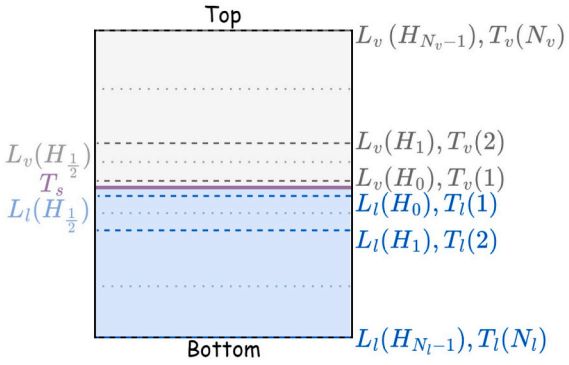

Fig. 26. Schematic of the discretised length scales in the liquid and vapour phase with respect to the tank

Heat transfer between saturated film and vapour and liquid phases (ET)

1

$$Q_{ET} = REFPROP\left(\rho_{v_{ET}}, u_{v_{ET}}(N_{v_{ET}})\right)$$

$$0 \leq Q_{ET} \leq 1$$

$$Pr_{v_{ET}} = REFPROP\left(T_{v_{ET}}(N_{v_{ET}}), Q_{ET} = 1\right) \qquad c_{v_{v_{ET}}} = REFPROP\left(T_{v_{ET}}(N_{v_{ET}}), Q_{ET} = 1\right)$$

$$\kappa_{v_{ET}} = REFPROP\left(T_{v_{ET}}(N_{v_{ET}}), Q_{ET} = 1\right) \qquad c_{p_{v_{ET}}} = REFPROP\left(T_{v_{ET}}(N_{v_{ET}}), Q_{ET} = 1\right)$$

$$\mu_{v_{ET}} = REFPROP\left(T_{v_{ET}}(N_{v_{ET}}), Q_{ET} = 1\right) \qquad \beta_{v_{ET}} = REFPROP\left(T_{v_{ET}}(N_{v_{ET}}), Q_{ET} = 1\right)$$

$$Q_{ET} > 1$$

$$Pr_{v_{ET}} = REFPROP\left(p_{v_{ET}}, u_{v_{ET}}(N_{v_{ET}})\right) \qquad c_{v_{v_{ET}}} = REFPROP\left(p_{v_{ET}}, u_{v_{ET}}(N_{v_{ET}})\right)$$

$$\kappa_{v_{ET}} = REFPROP\left(p_{v_{ET}}, u_{v_{ET}}(N_{v_{ET}})\right) \qquad c_{p_{v_{ET}}} = REFPROP\left(p_{v_{ET}}, u_{v_{ET}}(N_{v_{ET}})\right)$$

$$\mu_{v_{ET}} = REFPROP\left(p_{v_{ET}}, u_{v_{ET}}(N_{v_{ET}})\right) \qquad \beta_{v_{ET}} = REFPROP\left(p_{v_{ET}}, u_{v_{ET}}(N_{v_{ET}})\right)$$

$$Pr_{l_{ET}} = REFPROP\left(T_{l_{ET}}(N_{l_{ET}}), Q_{ET} = 0\right) \qquad c_{v_{l_{ET}}} = REFPROP\left(T_{l_{ET}}(N_{l_{ET}}), Q_{ET} = 0\right)$$

$$\kappa_{l_{ET}} = REFPROP\left(T_{l_{ET}}(N_{l_{ET}}), Q_{ET} = 0\right) \qquad c_{p_{l_{ET}}} = REFPROP\left(T_{l_{ET}}(N_{l_{ET}}), Q_{ET} = 0\right)$$

$$\mu_{l_{ET}} = REFPROP\left(T_{l_{ET}}(N_{l_{ET}}), Q_{ET} = 0\right) \qquad \beta_{l_{ET}} = REFPROP\left(T_{l_{ET}}(N_{l_{ET}}), Q_{ET} = 0\right)$$

2

$$L_{v_{min\,ET}} = \sqrt{\frac{\kappa_{v_{ET}} t_{min_{v_{ET}}}}{c_{p_{v_{ET}}} \rho_{v_{ET}}}} \qquad L_{v_{ET}}\left(H_{\frac{1}{2}}\right) = L_{v_{min\,ET}}$$

$$L_{v_{ET}}\left(H_{i+\frac{1}{2}}\right) = L_{v_{ET}}\left(H_{i-\frac{1}{2}}\right) e^{\frac{\pi}{\sqrt{N_{v_{ET}}}}} : i \in \{1, 2, \ldots, N_{v_{ET}} - 1\}$$

$$L_{v_{ET}}(H_0) = \frac{L_{v_{min\,ET}}}{1 + e^{\left(\frac{\pi}{2\sqrt{N_{v_{ET}}}}\right)}} \qquad L_{v_{ET}}(H_i) = \sqrt{L_{v_{ET}}\left(H_{i-\frac{1}{2}}\right) \cdot L_{v_{ET}}\left(H_{i+\frac{1}{2}}\right)} : i \in \{1, 2, \ldots, N_{v_{ET}} - 1\}$$

3

$$L_{l_{min\,ET}} = \sqrt{\frac{\kappa_{l_{ET}} t_{min_{l_{ET}}}}{c_{p_{l_{ET}}} \rho_{l_{ET}}}} \qquad L_{l_{ET}}\left(H_{\frac{1}{2}}\right) = L_{l_{min\,ET}}$$

$$L_{l_{ET}}\left(H_{i+\frac{1}{2}}\right) = L_{l_{ET}}\left(H_{i-\frac{1}{2}}\right) e^{\frac{\pi}{\sqrt{N_{l_{ST}}}}}\, i \in \{1, 2, \ldots, N_{l_{ET}} - 1\}$$

$$L_{l_{ET}}(H_0) = \frac{L_{l_{min\,ET}}}{1 + e^{\left(\frac{\pi}{2\sqrt{N_{l_{ET}}}}\right)}} \qquad L_{l_{ET}}(H_i) = \sqrt{L_{l_{ET}}\left(H_{i-\frac{1}{2}}\right) \cdot L_{l_{ET}}\left(H_{i+\frac{1}{2}}\right)} i \in \{1, 2, \ldots, N_{l_{ET}} - 1\}$$

4

$$\alpha_{vs_{ET_{cond}}} = \frac{\kappa_{v_{ET}}}{L_{v_{ET}}\left(H_{\frac{1}{2}}\right)} \qquad h_{ls_{ET_{cond}}} = \frac{\kappa_{l_{ET}}}{L_{l_{ET}}\left(H_{\frac{1}{2}}\right)}$$

$$\alpha_{vs_{ET_{conv}}} = \frac{\kappa_{v_{ET}} Nu_{vs_{ET_{conv}}}}{L} \qquad h_{ls_{ET_{conv}}} = \frac{\kappa_{l_{ET}} Nu_{ls_{ET_{conv}}}}{L}$$

$$Nu_{vs_{ET_{conv}}} = 0.156 (Ra_{vs_{ET}})^{\frac{1}{3}} \qquad Nu_{ls_{ET_{conv}}} = 0.156 (Ra_{ls_{ET}})^{\frac{1}{3}}$$

$$Ra_{vs_{ET}} = \frac{g \beta_{v_{ET}} \left(T_{s_{ET}} - T_{v_{ET}}(N_{v_{ET}})\right) L^3 Pr_{v_{ET}}}{\nu_{v_{ET}}^2} \qquad Ra_{ls_{ET}} = \frac{g \beta_{l_{ET}} \left(|T_{l_{ET}} - T_{s_{ET}}(N_{l_{ET}})|\right) L^3 Pr_{l_{ET}}}{\nu_{l_{ET}}^2}$$

$$\alpha_{vs_{ET_{conv}}} = \frac{\kappa_{v_{ET}} \cdot 0.156 (Ra_{vs_{ET}})^{\frac{1}{3}}}{L} \qquad \alpha_{ls_{ET_{conv}}} = \frac{\kappa_{l_{ET}} \cdot 0.156 (Ra_{ls_{ET}})^{\frac{1}{3}}}{L}$$

5

$$\dot{Q}_{vs_{ET_{cond}}} = \alpha_{vs_{ET_{cond}}} S_{l,v-interface_{ET}} \left(T_{v_{ET}}(H_0) - T_{s_{ET}}\right) - L_{v_{ET}}(H_0) c_{v_{v_{ET}}} \rho_{v_{ET}} \frac{dT_{s_{ET}}}{dt}$$

$$\dot{Q}_{vs_{ET_{conv}}} = \alpha_{vs_{ET_{conv}}} S_{l,v-interface_{ET}} \left(T_{v_{ET}}(H_0) - T_{s_{ET}}\right) H\left(T_{s_{ET}} - T_{v_{ET}}(N_{v_{ET}})\right)$$

$$\dot{Q}_{vs_{ET}} = min\{\dot{Q}_{vs_{ET_{cond}}}, \dot{Q}_{vs_{ET_{conv}}}\}$$

$$\dot{Q}_{ls_{ET_{cond}}} = \alpha_{ls_{ET_{cond}}} S_{l,v-interface_{ET}} \left(T_{l_{ET}}(H_0) - T_{s_{ET}}\right) - L_{l_{ET}}(H_0) c_{p_{l_{ET}}} \rho_{l_{ET}} \frac{dT_{s_{ET}}}{dt}$$

$$\dot{Q}_{ls_{ET_{conv}}} = \alpha_{ls_{ET_{conv}}} S_{l,v-interface_{ET}} \left(T_{l_{ET}}(H_0) - T_{s_{ET}}\right) H\left(T_{l_{ET}}(N_{l_{ET}}) - T_{s_{ET}}\right)$$

$$\dot{Q}_{ls_{ET}} = max\{\dot{Q}_{ls_{ET_{cond}}}, \dot{Q}_{ls_{ET_{conv}}}\}$$

Fig. 27. Heat transfer between saturated film and vapour and liquid phases (ET)

A.10. Heat Transfer between the Wall and Vapour and Liquid Phases (ET)

The heat transfer between the wall and the vapour and liquid phases in the ET is now evaluated, for which the formulas are shown in Fig. 28. Detailed explanation is now given.

1. First, the kinematic viscosity of the vapour is calculated. The Rayleigh number for the vapour is calculated by equation (A4) in Ref. [18], for which the typical length is the height of the ullage. The coefficient of convective heat transfer for the vapour connected to the side of the tank is based on

   Equation (A3) of [18], so that $Nu = 0.68 + 0.503(Ra \cdot \Psi)^{\frac{1}{4}}$, where Ψ is calculated using Equation A6) from Ref. [18].

2. The kinematic viscosity of the liquid is then calculated. Again, the Rayleigh number for the vapour is calculated by equation (A4) in Ref. [18], for which the typical length is now the height of the liquid.

   The convective heat transfer coefficient for the liquid is based on equation (A3) from Ref. [18], so that.

   $Nu = 0.68 + 0.503(Ra \cdot \Psi)^{\frac{1}{4}}$, where Ψ is again calculated using equation (A6) from Ref. [18]. For the bottom, the Rayleigh number for the vapour is once again calculated by equation (A4) in Ref. [18], for which the typical length is now the diameter of the external tank. Then, the Nusselt number for the bottom is computed using an empirical relation from DeWitt et al. (1990) [42] for natural convection of the upper surface of a cold plate $Nu = 0.27(Ra)^{\frac{1}{4}}$, which is used to calculate the convective heat transfer along the bottom in the liquid.

3. The heat transfer between the wall and the liquid and the vapour is calculated according to equation (17) of [18]. For the vapour, both the area of the wall subjected to the vapour and the top of the tank are considered by the same heat transfer coefficient. For the liquid, also the wall and the bottom are considered, but a different heat transfer coefficient is used as calculated in the former step.

Heat transfer between the wall and vapour and liquid phases (ET)

1

$$\nu_{v_{ET}} = \frac{\mu_{v_{ET}}}{\rho_{v_{ET}}}$$

$$Ra_{v_{ET_{side}}} = \frac{g\beta_{v_{ET}}\left(\left|T_{w_{ET}} - T_{v_{ET}}\left(N_{v_{ET}}\right)\right|\right)\left(H_{ET} - H_{l_{ET}}\right)^3 Pr_{v_{ET}}}{\nu_{v_{ET}}^2}$$

$$\Psi_{v_{ET_{side}}} = \left[1 + \left(\frac{0.492}{Pr_{v_{ET}}}\right)^{\frac{9}{16}}\right]^{\frac{-16}{9}}$$

$$Nu_{v_{ET_{side}}} = 0.68 + 0.503\left(Ra_{v_{ET_{side}}} \cdot \Psi_{v_{ET_{side}}}\right)^{\frac{1}{4}}$$

$$\alpha_{v_{ET_{side}}} = \frac{Nu_{v_{ET_{side}}} \kappa_{v_{ET}}}{H_{ET} - H_{l_{ET}}}$$

2

$$\nu_{l_{ET}} = \frac{\mu_{l_{ET}}}{\rho_{l_{ET}}}$$

$$Ra_{l_{ET_{side}}} = \frac{g\beta_{l_{ET}}\left(\left|T_{w_{ET}} - T_{l_{ET}}\left(N_{l_{ET}}\right)\right|\right)H_{l_{ET}}^3 Pr_{l_{ET}}}{\nu_{l_{ET}}^2}$$

$$\Psi_{l_{ET_{side}}} = \left[1 + \left(\frac{0.492}{Pr_{l_{ET}}}\right)^{\frac{9}{16}}\right]^{\frac{-16}{9}}$$

$$Nu_{l_{ET_{side}}} = 0.68 + 0.503\left(Ra_{l_{ET_{side}}} \cdot \Psi_{l_{ET_{side}}}\right)^{\frac{1}{4}}$$

$$\alpha_{l_{ET_{side}}} = \frac{Nu_{l_{ET_{side}}} \kappa_{l_{ET}}}{H_{l_{ET}}}$$

$$Ra_{l_{ET_{bottom}}} = \frac{g\beta_{l_{ET}}\left(T_{w_{ET}} - T_{l_{ET}}\left(N_{l_{ET}}\right)\right)\left(2R_{ET}\right)^3 Pr_{l_{ET}}}{\nu_{l_{ET}}^2}$$

$$Nu_{l_{ET_{bottom}}} = 0.27\left(Ra_{l_{ET_{bottom}}}\right)^{\frac{1}{4}}$$

$$\alpha_{l_{ET_{bottom}}} = \frac{Nu_{l_{ET_{bottom}}} \kappa_{l_{ET}}}{2R_{ET}}$$

3

$$\dot{Q}_{wv_{ET}} = \left(T_{w_{ET}} - T_{v_{ET}}\left(N_{v_{ET}}\right)\right) \cdot \alpha_{v_{ET_{side}}} \cdot \left(2\pi R_{ET}\left(H - H_{l_{ET}}\right) + S_{ET_{bottom}}\right)$$

$$\dot{Q}_{wl_{ET}} = \left(T_{w_{ET}} - T_{l_{ET}}\left(N_{l_{ET}}\right)\right)\left(\alpha_{l_{ET_{bottom}}} S_{ET_{bottom}} + \alpha_{l_{ET_{side}}} \cdot 2\pi R_{ET} H_{l_{ET}}\right)$$

Fig. 28. Heat transfer between the wall and vapour and liquid phases (ET)

A.11. Condensation Flow (ET)

The condensation flows in the ET are determined, for which the formulas are shown in Fig. 29 and an explanation is now provided.

1. The enthalpy of vaporisation is computed for ET as a function of the saturated film temperatures using a correlation.
2. The mass flow rate over the saturated film due to condensation in the ET is displayed in Fig. 29 and calculated according to equation (14) of [18].

Condensation flow (ET)

1

$$h_{vap_{ET}} = f(T_{s_{ET}})$$

2

$$J_{cd_{ET}} = -\frac{\left(\dot{Q}_{ls_{ET}} + \dot{Q}_{vs_{ET}}\right)}{h_{vap_{ET}}}$$

Fig. 29. Condensation flows in the ET

A.12. Mass Balances (ST) and (ET)

The mass balances are displayed in Fig. 31 and the corresponding equations are shown in Fig. 30 and are derived from Fig. 1. These are now discussed step by step.

1. The mass flow rates for the stationary tank are shown in Fig. 31a. The mass flow rate of the vapour is computed by considering the conservation of mass in the vapour. The same principle holds for the liquid.
2. The mass flow rates for the external tank are shown in Figd. 31b. Again, the mass flow rate of the vapour is computed by considering the conservation of mass in the vapour. The same principle holds for the liquid.
3. The pressure-volume work rate is calculated as $\dot{W} = -P_{external}\Delta\dot{V}$. The external pressure is the vapour pressure.
4. The velocities of the vapour leaving the vent lines are now calculated. It should be noted that S_{vent} is the cross-sectional area of the orifice area of the corresponding vent valves.
5. The specific enthalpies in the ST are determined. For the transfer line at the exit of the ST, the specific enthalpy is obtained using REFPROP based on the liquid temperature in the bottom node and a quality of zero. The condensation enthalpy is determined by REFPROP based on the film saturation temperature and a quality of 1. Finally, the specific enthalpy at the exit of the ST vent line is calculated using REFPROP on the basis of the vapour temperature in the top node and the vapour density.
6. The specific enthalpies in the ET are determined. The condensation enthalpy is determined by REFPROP based on the film saturation temperature and a quality of 1. Finally, the specific enthalpy at the entrance of the ET vent line is calculated using REFPROP on the basis of the vapour temperature in the top node and the vapour density.
7. The specific enthalpy of the at the interface between the vapour hydrogen and the boiling hydrogen after the vapourizer is determined by REFPROP based on a considered boiling temperature and a quality of 1.

Mass balances (ST) and (ET)

$J_{v_{ST}} = J_{boil} - J_{vent_{ST}} - J_{cd_{ST}}$ $J_{l_{ST}} = -J_{tr} - J_{vap} - +J_{cd_{ST}}$	1	$J_{v_{ET}} = r_{top-to-bottom} \cdot J_{tr} - J_{vent_{ET}} - J_{cd_{ET}}$ $J_{l_{ET}} = (1 - r_{top-to-bottom}) \cdot J_{tr} + J_{cd_{ET}}$	2
$pd\dot{V}_{ST} = -p_{v_{ST}} \left(\frac{J_{l_{ST}}}{\rho_{l_{ST}}} \right)$ $\quad pd\dot{V}_{ET} = -p_{v_{ET}} \left(\frac{J_{l_{ET}}}{\rho_{l_{ET}}} \right)$			3
$v_{vent_{ST}} = \frac{J_{vent_{ST}}}{S_{vent_{ST}} \rho_{v_{ST}}}$ $\quad v_{vent_{ET}} = \frac{J_{vent_{ET}}}{S_{vent_{ET}} \rho_{v_{ET}}}$			4
$h_{tr_{ST}} = REFPROP\left(T_{l_{ST}}(N_{l_{ST}}), Q_{ST} = 0\right)$ $h_{cd_{ST}} = REFPROP\left(T_{s_{ST}}, Q_{ST} = 1\right)$ $h_{vent_{ST}} = REFPROP\left(T_{v_{ST}}(N_{v_{ST}}), \rho_{v_{ST}}\right)$	5	$h_{cd_{ET}} = REFPROP\left(T_{s_{ET}}, Q_{ET} = 1\right)$ $h_{vent_{ET}} = REFPROP\left(T_{v_{ET}}(N_{v_{ET}}), \rho_{v_{ET}}\right)$	6
$h_{boil} = REFPROP\left(T_{boil}, Q_{ST} = 1\right)$			7

Fig. 30. Mass balances (ST) and (ET)

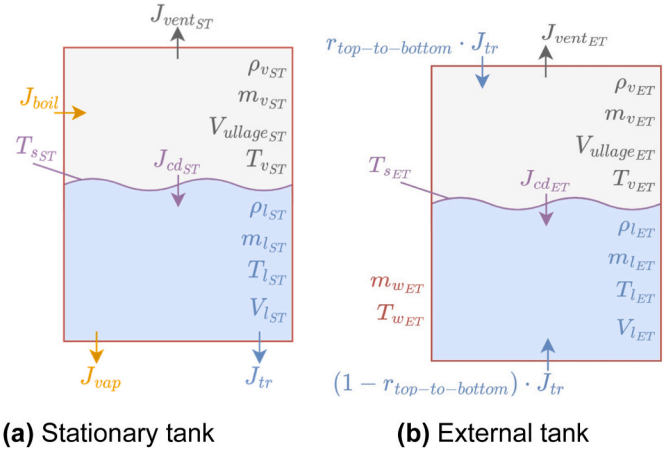

Fig. 31. Mass transfer

A.13. Heat Flows to Vapour and Liquid Phases in (ST)

The energy balance in the ST is shown in Fig. 34a and the corresponding equations are listed in Fig. 32.

1. The velocity in the transfer line is determined.
2. The heat transfer into the vapour is calculated using the conservation of energy in this phase.

The same principle is applied for the liquid phase.

Heat flows to vapour and liquid phases in (ST)

$$v_{tr} = \frac{J_{tr}}{S_{tr}\rho_{tr}} \quad (1)$$

$$\dot{Q}_{v_{ST}} = \dot{Q}_{ev_{ST}} - \dot{Q}_{vs_{ST}} - pd\dot{V}_{ST} - J_{vent_{ST}}\left(h_{vent_{ST}} + \frac{v^2_{vent_{ST}}}{2}\right) - J_{cd_{ST}}h_{cd_{ST}} + J_{boil}h_{boil}$$

$$\dot{Q}_{l_{ST}} = \dot{Q}_{el_{ST}} - \dot{Q}_{ls_{ST}} + pd\dot{V}_{ST} - J_{tr_{ST}}\left(h_{tr_{ST}} + \frac{v^2_{tr}}{2}\right) + J_{cd_{ST}}h_{cd_{ST}} - J_{vap}h_{tr_{ST}} \quad (2)$$

Fig. 32. Heat flows to vapour and liquid phases in (ST)

A.14. Heat Flows to Vapour and Liquid Phases in (ET)

The energy balance in the ET is shown in Fig. 34b and the corresponding equations are listed in Fig. 33. The heat transfer into the vapour is determined by applying the conservation of energy, which is also done for the liquid phase to obtain the heat transfer into the liquid.

Heat flows to vapour and liquid phases in (ET)

$$\dot{Q}_{v_{ET}} = \dot{Q}_{wv_{ET}} - \dot{Q}_{vs_{ET}} - pd\dot{V}_{ET} + r_{top-to-bottom}J_{tr}\left(h_{tr_{ST}} + \frac{v^2_{tr}}{2} - h_{vap_{ET}}\right) - J_{vent_{ET}}\left(h_{vent_{ET}} + \frac{v^2_{vent_{ET}}}{2}\right) - J_{cd_{ET}}h_{cd_{ET}}$$

$$\dot{Q}_{l_{ET}} = \dot{Q}_{wv_{ET}} - \dot{Q}_{ls_{ET}} + pd\dot{V}_{ET} + (1 - r_{top-to-bottom})J_{tr}\left(h_{tr_{ST}} + \frac{v^2_{tr}}{2}\right) + J_{cd_{ET}}h_{cd_{ET}}$$

Fig. 33. Heat flows to vapour and liquid phases in (ET)

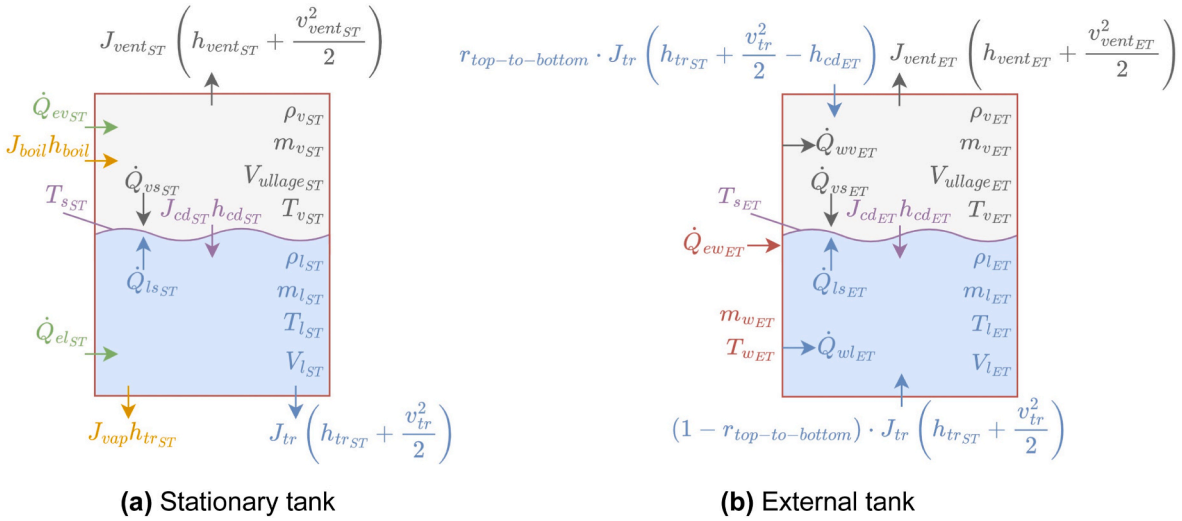

Fig. 34. Energy transfer

A.15. Variation of Internal Energies

The heat conduction equation in the Cartesian coordinate system is displayed in Eq. (38) [33], where q^* is the generation of specific internal heat per unit volume and c is the specific heat.

$$\kappa\left[\frac{\partial^2 T}{\partial x^2} + \frac{\partial^2 T}{\partial y^2} + \frac{\partial^2 T}{\partial z^2}\right] + \dot{q}^* = \rho c\frac{\partial T}{\partial t} \quad (38)$$

Since the nodes in the vapour and liquid phases are one-dimensional and there is no internal heat generation, Eq. (38) can be reduced to Eq. (39).

$$\kappa\left[\frac{\partial^2 T}{\partial x^2}\right] = \rho c\frac{\partial T}{\partial t} \quad (39)$$

Eq. (39) can be rewritten so that the state derivative of the temperature is obtained in Eq. (40).

$$\frac{\partial T}{\partial t} = \frac{\kappa}{\rho c}\left[\frac{\partial^2 T}{\partial x^2}\right] \quad (40)$$

The specific internal energy is considered to be proportional to its temperature, so that $u \cong cT$. Using this relation, Eq. (40) can be transformed to the state derivative of the internal energy as shown in Eq. (41).

$$\frac{\partial u}{\partial t} = \frac{\kappa}{\rho}\left[\frac{\partial^2 T}{\partial x^2}\right] = \frac{\kappa}{\rho}\frac{\partial}{\partial x}\left(\frac{\partial T}{\partial x}\right) \tag{41}$$

$\frac{\partial T}{\partial x}$ can be approximated using the central difference method. The equations for the variation of the internal energies in the vapour and liquid nodes of both ST and ET are shown in Fig. 35. The calculations are explained in the following. Again, the relation between the discretised length scales and the number of nodes is shown in Fig. 7.

1. The state derivative for the top vapour node in the ET (N_{vET}) was determined by comparing the calculated heat flow in the vapour phase to the current heat flow in this node.
2. The state derivative for the bottom liquid node in the ET (N_{lET}) was determined by comparing the calculated heat flow into the liquid phase with the current heat flow in this node.

Variation of internal energies (ET)

1

$$T_{v_{ET}}(0) = T_{s_{ET}}$$
$$\rho_{v_{i_{ET}}}(i) = REFPROP\left(p_{v_{ET}}, u_{v_{ET}}(i)\right) : i \in \{1, 2, \ldots, N_{v_{ET}} - 1\}$$
$$\frac{du_{v_{ET}}(i)}{dt} = \left(\frac{T_{v_{ET}}(i+1) - T_{v_{ET}}(i)}{L_{v_{ET}}\left(H_{i+\frac{1}{2}}\right)} - \frac{T_{v_{ET}}(i) - T_{v_{ET}}(i-1)}{L_{v_{ET}}\left(H_{i-\frac{1}{2}}\right)}\right) \cdot \left(\frac{\kappa_{v_{ET}}}{L_{v_{ET}}(H_{i-1})\rho_{v_{i_{ET}}}(i)}\right) : i \in \{1, 2, \ldots, N_{v_{ET}} - 1\}$$
$$u_{v_{ET}}(N_{v_{ET}}) = REFPROP\left(T_{v_{ET}}(N_{v_{ET}}), \rho_{v_{ET}}\right)$$
$$\frac{du_{v_{ET}}(N_{v_{ET}})}{dt} = \dot{Q}_{v_{ET}} - \frac{J_{v_{ET}} \cdot u_{v_{ET}}(N_{v_{ET}})}{m_{v_{ET}}}$$

2

$$T_{l_{ET}}(0) = T_{s_{ET}}$$
$$\rho_{l_{i_{ET}}}(i) = REFPROP\left(T_{l_{ET}}(i), Q_{ET} = 0\right) : i \in \{1, 2, \ldots, N_{l_{ET}} - 1\}$$
$$\frac{du_{l_{ET}}(i)}{dt} = \left(\frac{T_{l_{ET}}(i+1) - T_{l_{ET}}(i)}{L_{l_{ET}}\left(H_{i+\frac{1}{2}}\right)} - \frac{T_{l_{ET}}(i) - T_{l_{ET}}(i-1)}{L_{l_{ET}}\left(H_{i-\frac{1}{2}}\right)}\right) \cdot \left(\frac{\kappa_{l_{ET}}}{L_{l_{ET}}(H_{i-1})\rho_{l_{i_{ET}}}(i)}\right) : i \in \{1, 2, \ldots, N_{l_{ET}} - 1\}$$
$$u_{l_{ET}}(N_{l_{ET}}) = REFPROP\left(T_{l_{ET}}(N_{l_{ET}}), \rho_{l_{ET}}\right)$$
$$\frac{du_{l_{ET}}(N_{l_{ET}})}{dt} = \dot{Q}_{l_{ET}} - \frac{J_{l_{ET}} \cdot u_{l_{ET}}(N_{l_{ET}})}{m_{l_{ET}}}$$

Fig. 35. Variation of internal energies

A.16. ET Wall Temperature

The equations for the wall temperature in the external tank are shown in Fig. 36. $c_{w_{tr}}$ and $\frac{dc_{w_{tr}}}{dT}$ are material properties, which were already identified for stainless steel 304. $\dot{Q}_{ew_{tr}}$ can be obtained from experimental data or by assuming a certain heat inflow.

ET wall temperature

$$\frac{dc_{w_{ET}}}{dT} = f\left(T_{w_{ET}}\right) \qquad c_{w_{ET}} = f\left(T_{w_{ET}}\right) \qquad \dot{Q}_{ew_{ET}} = f\left(V_{l_{ET}}\right) \qquad \frac{dT_{w_{ET}}}{dt} = \frac{\dot{Q}_{ew_{ET}} - \dot{Q}_{wl_{ET}} - \dot{Q}_{wv_{ET}}}{m_{w_{ET}}\left(c_{w_{ET}} + \left(T_{w_{ET}} \cdot \frac{dc_{w_{ET}}}{dT}\right)\right)}$$

Fig. 36. ET wall temperature

A.17. Tank Wall

In contrast to Petitpas' model, a distinction was made between the part of the receiving tank wall that is in contact with the ullage and the liquid, which is in line with the original NASA model [19]. As the temperature of the ullage is likely higher than the liquid temperature, a temperature gradient is expected in the tank wall, resulting in conduction in the tank wall. Like in the Petitpas' model, both the temperature of the tank wall in contact with the ullage and the liquid are assumed uniform.

A.18. Conduction

Using the one-dimensional thermal resistance shown in Fig. 37a, the heat transfer due to conduction can be calculated using Eq. (42), where $T_1 = T_{w,vapour}$ and $T_2 = T_{w,liquid}$.

$$\dot{Q}_{w,cond} = \frac{T_1 - T_2}{R} \tag{42}$$

The thermal resistances of the two parts of the wall are in series, so that Eq. (43) holds.

$$R = R_1 + R_2 \tag{43}$$

The thermal resistance equation for conduction is shown in Eq. (44).

$$R = \frac{L}{\kappa S} \tag{44}$$

Combining Eq. (42), Eq. (43) and Eq. (44) resulted in Eq. (45), where $\kappa_1 = \kappa(T_1)$, $\kappa_2 = \kappa(T_2)$ and $S{=}S_1{=}S_2$, as indicated in Fig. 37b. L_1 and L_2 are determined by taking the midpoint of the distance between the liquid/vapour interface and the top and bottom of the tank for the vapour and liquid phase, respectively, shown in Fig. 37c.

$$\dot{Q}_{w,cond} = \frac{T_1 - T_2}{\left(\frac{L_1}{\kappa_1 S_1}\right) + \left(\frac{L_2}{\kappa_2 S_2}\right)} \tag{45}$$

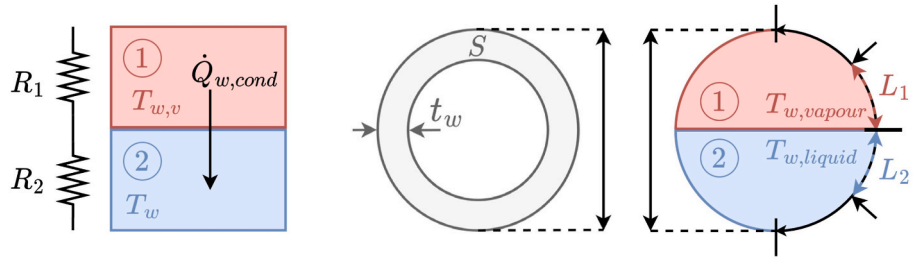

(a) Thermal resistance model **(b)** Cross-sectional area **(c)** Conduction lengths

Fig. 37. Conduction in the tank wall

A.19. Time Derivative for Tank Wall

To take into account the thermal mass, a similar approach was considered as suggested by Petitpas, which was discussed in detail in Section A.16. However, since the wall temperature is now modelled as consisting of two different temperatures with conduction as result, some modifications were implemented, as shown in Eq. (46). $\dot{Q}_{w,cond}$ is + for the part of the tank wall that is in contact with the liquid and − for the part that is in contact with the ullage.

$$\begin{aligned} m_{w,l/v}\frac{d\left(c_{w,l/v}T_{w,l/v}\right)}{dt} &= \dot{Q}_{ew,l/v} - \dot{Q}_{w,l/v} \pm \dot{Q}_{w,cond} \\ \frac{d\left(c_{w,l/v}T_{w,l/v}\right)}{dt} &= \frac{\dot{Q}_{ew,l/v} - \dot{Q}_{w,l/v} \pm \dot{Q}_{w,cond}}{m_{w,l/v}} \end{aligned} \tag{46}$$

Using the product rule of differentiation, Eq. (47) is obtained.

$$\frac{dT_{w,l/v}}{dt}c_{w,l/v} + \frac{dc_{w,l/v}}{dt}T_{w,l/v} = \frac{\dot{Q}_{ew,l/v} - \dot{Q}_{w,l/v} \pm \dot{Q}_{w,cond}}{m_{w,l/v}} \tag{47}$$

Again, as the heat capacity is a function of temperature and not of time, the chain rule was used as indicated in Eq. (48).

$$\frac{dT_{w,l/v}}{dt}c_{w,l/v} + \frac{dc_{w,l/v}}{dT}\frac{dT_{w,l/v}}{dt}T_{w,l/v} = \frac{\dot{Q}_{ew,l/v} - \dot{Q}_{w,l/v} \pm \dot{Q}_{w,cond}}{m_{w,l/v}} \tag{48}$$

To obtain the transient wall time derivatives for the temperature of the receiving wall in contact with the liquid and the ullage, Eq. (48) was rewritten to Eq. (49), where $\dot{Q}_{w,cond}$ was derived in Eq. (45).

$$\frac{dT_{w,l/v}}{dt} = \frac{\dot{Q}_{ew,l/v} - \dot{Q}_{w,l/v} \pm \dot{Q}_{w,cond}}{m_{w,l/v}\left(c_{w,l/v} + \left(\frac{dc_{w,l/v}}{dT}T_{w,l/v}\right)\right)} \tag{49}$$

B. Model Inputs

Table 6
Inputs for the tank model modification and validation

General Value Transfer Line			Value
fluid	REFPROP::PARAHYD	Dtr	2.54E-02
p_atm	1.01E+05	Ltr	0.2
T_amb	288.00	drtr	1.00E-06
g	9.81	tau_tr	5

(*continued on next page*)

Table 6 (*continued*)

General Value Transfer Line			Value
psiToPa	6894.76	dE	1.27E-02
sigma	5.67E-08	kE	11
		Aircraft Tank	Value
		VTotal2	1.39
T_c	32.94		
p_c	1.32E+06		
Lambda	5.00	tw2	1.00E-03
DD	6.00E-03	R2	0.69
Dti_DD	0.80	epsilon2	0.16
nL1	11.00	H2	1.37
tminL1	0.10	p20	1.16E+05
nL2	11.00	Tv20	20.86
tminL2	0.10	TL20	20.98
nV1	11.00	TwL20	32.77
tminV1	0.10	Twv20	32.77
nV2	11.00	pct_VL20	0.45
tminV2	0.10	Ts20	20.28
tStart	179.00	VL20	0.63
tFinal	600.00	hL20	0.65
relTol	1.00E-04	rhoL20	70.27
Supply Tank Value		mL20	43.96
VTotal1	5.68	rhov20	1.51
R1	0.80	mv20	1.15
A1	2.01	ratio_top_bottom	1.00
Lcyl1	2.82	mw2	40.37
p10	3.38E+05	MaterialTank2	Aluminum5083
TL10	25.12	S_valve2	3.84E-04
Tv10	25.21	ETVentState	0.00
rhov10	4.09	p_ET_low	3.00 + 05
rhoL10	64.29	p_ET_high	3.35E+05
pct_VL10 totalmass10	0.80	TopET	0.85
	292.05		
Vullage10	1.21		
mL10	292.05		
mv10	4.64		
Ts10	25.09		
Jboil0	3.00E-02		
Jtr0	4.10E-01		
Qdotconstant1	5.49		
mVap0	3.00E-02		
Tboil	25.12		
tau_vap	0.20		
c_vap	5.00E-05		
VapValveState	0		
S_valve1	3.84E-04		
STVentState	0		
p_ST_fill	3.39E+05		

References

[1] Abrantes I, Ferreira AF, Silva A, Costa M. Sustainable aviation fuels and imminent technologies - CO_2 emissions evolution towards 2050. J Clean Prod 2021;313:127–937. https://doi.org/10.1016/j.jclepro.2021.127937. ISSN: 0959-6526.

[2] Graver B, Zhang K, Rutherford D. Emissions from commercial aviation. ICCT; 2018. 2019.

[3] Barrett SR, Britter RE, Waitz IA. Global mortality attributable to aircraft cruise emissions. Environ Sci Technol 2010;44(19):7736–42.

[4] Grewe V, Gangoli Rao A, Grönstedt T, Xisto C, Linke F, Melkert J, Middel J, Ohlenforst B, Blakey S, Christie S, et al. Evaluating the climate impact of aviation emission scenarios towards the paris agreement including covid-19 effects. Nat Commun 2021;12(1):3841.

[5] Fleming GG, Lépinay Id, Schaufele R. Environmental trends in aviation to 2050. https://www.icao.int/environmentalprotection/Documents/EnvironmentalReports/2022/ENVReport2022_Art7.pdf. [Accessed 9 November 2023].

[6] Yusaf T, Fernandes L, Abu Talib AR, Altarazi YS, Alrefae W, Kadirgama K, Ramasamy D, Jayasuriya A, Brown G, Mamat R, et al. Sustainable aviation—hydrogen is the future. Sustainability 2022;14(1):548.

[7] Brewer GD. Hydrogen aircraft technology. CRC Press, Inc.; 1991.

[8] Department Boeing PD, Aeronautics National, Administration Space. *An exploratory Study to determine the integrated technological air transportation System ground requirements of liquid-hydrogen-fueled subsonic, long-haul civil air transports* (NASA contractor report). National Aeronautics and Space Administration; 1976 [Online]. Available: https://books.google.nl/books?id=pJBSBZvbP5QC.

[9] Clean Aviation Joint Undertaking. Hydrogen powered aviation: a fact-based study of hydrogen technology, economics, and climate impact by 2050. 2020. https://doi.org/10.2843/766989. 978-92-9246-341-0.

[10] Mangold J, Silberhorn D, Moebs N, Dzikus N, Hoelzen J, Zill T, Strohmayer A. Refueling of LH2 Aircraft—Assessment of turnaround procedures and aircraft design implication. Energies 2022;15(7):2475.

[11] Clean Aviation 2 JU, FCH JU. "A fact-based study of hydrogen technology, economics, and climate impact by 2050,". Fuel cell and hydrogen joint Undertaking; IGEM. 2020. Boston, MA, USA.

[12] Darr S, Hartwig J, Dong J, Wang H, Majumdar A, LeClair A, Chung J. Two-phase pipe quenching correlations for liquid nitrogen and liquid hydrogen. J Heat Tran 2019;141(4).

[13] Majumdar A, Van Hooser K. A generalized fluid system simulation program to model secondary flows in turbomachinery. 31st joint propulsion conference, 2969. AIAA Paper; 1995.

[14] Cullimore B, Ring S, Johnson D. Sinda/fluint general purpose thermal/fluid network analyzer. User's Manual 2006;5.

[15] Hartwig J, Darr S, Asencio A. Assessment of existing two-phase heat transfer coefficient and critical heat flux correlations for cryogenic flow boiling in pipe quenching experiments. Int J Heat Mass Tran 2016;93:441–63.

[16] Al Ghafri SZ, Swanger A, Jusko V, Siahvashi A, Perez F, Johns ML, May EF. Modelling of liquid hydrogen boil-off. Energies 2022;15(3):1149.

[17] Petitpas G. Simulation of boil-off losses during transfer at a lh2 based hydrogen refueling station. Int J Hydrogen Energy 2018;43(46):21 451–21 463.

[18] Osipov VV, Daigle MJ, Muratov CB, Foygel M, Smelyanskiy VN, Watson MD. Dynamical model of rocket propellant loading with liquid hydrogen. J Spacecraft Rockets 2011;48(6):987–98.

[19] Daigle M., Foygel M., Smelyanskiy V., Boschee J. LH2sim [computer software] 2017. [Online]. Available: https://github.com/nasa/LH2Sim. [Accessed 9 November 2023].
[20] Petitpas G. Lh2 transfer simulation. https://github.com/LLNL/LH2Transfer. [Accessed 9 November 2023].
[21] Daigle MJ, Smelyanskiy VN, Boschee J, Foygel M. Temperature stratification in a cryogenic fuel tank. J Thermophys Heat Tran 2013;27(1):116–26.
[22] Hartwig J, Moore R, Mercado M. Test data analysis of the liquid hydrogen chilldown and fill transfer experiments on a flight weight aluminum tank. Int J Heat Mass Tran 2023;202:123–766.
[23] Lloyd JR, Moran WR. Natural convection adjacent to horizontal surface of various planforms. J Heat Tran Nov. 1974;96(4):443–7. https://doi.org/10.1115/1.3450224. ISSN: 0022-1481.
[24] Churchill SW, Chu HH. Correlating equations for laminar and turbulent free convection from a vertical plate. Int J Heat Mass Tran 1975;18(11):1323–9. https://doi.org/10.1016/0017-9310(75)90243-4. ISSN: 0017-9310.
[25] Shashi Menon E. Chapter five - fluid flow in pipes. In: Shashi Menon E, editor. Transmission pipeline calculations and simulations manual. Boston: Gulf Professional Publishing; 2015. p. 149–234. https://doi.org/10.1016/B978-1-85617-830-3.00005-5. 978-1-85617-830-3.
[26] Churchill SW. Friction-factor equation spans all fluid-flow regimes. 1977.
[27] Corberan J, Gonzalvez J, Fuentes D. Calculation of refrigerant properties by linear interpolation of bidimensional meshes. In: Proceedings of IIR international conference of thermophysical properties and transport process of refrigerants, August 31September 2, Vicenza, Italy; 2005.
[28] Wang C, Ju Y. Modeling, simulation and analysis of tank thermodynamic behaviors during no-venting bunkering operations. Cryogenics 2021;120:103–373.
[29] Arifien BN, Zarrouk SJ, Kurniawan W. Scrubbing lines in geothermal power generation systems. In: Proceeding the 37th New Zealand geothermal workshop; 2015.
[30] Bergman TL, Bergman TL, Incropera FP, Dewitt DP, Lavine AS. Fundamentals of heat and mass transfer. John Wiley & Sons; 2011.
[31] Brauer H. Momentum, mass, and heat-transfer through boundary surface of spherical-particles. Chem Ing Tech 1973;45(18):1099–103.
[32] Deng C, Huang W, Wang H, Cheng S, He X, Xu B. Preparation of micron-sized droplets and their hydrodynamic behavior in quiescent water. Braz J Chem Eng 2018;35:709–20.
[33] Schmidt FW, Henderson RE, Wolgemuth CH. Introduction to thermal sciences. JOHN WILEY & SONS, INC.; 1984. 605 THIRD AVE., NEW YORK, NY 10158, USA, 1984, 448.
[34] Weisstein EW. Spherical cap. https://mathworld.wolfram.com/SphericalCap.html. [Accessed 9 November 2023].
[35] Lebrun P. An introduction to cryogenics. CERN-AT-2007-001. CERN; Jan. 2007. https://doi.org/10.17181/CERN.KOEP.SD6C.
[36] Chen W, Gao R, Sun J, Lei Y, Fan X. Modeling of an isolated liquid hydrogen droplet evaporation and combustion. Cryogenics May 2018;96. https://doi.org/10.1016/j.cryogenics.2018.05.012.
[37] Adam A, He W, Fan Y, Han D. Investigation of flow characteristics and mixing of liquid hydrogen within a premixing swirl tube for the turbine engine combustor. Int J Hydrogen Energy 2024;49:367–83. https://doi.org/10.1016/j.ijhydene.2023.07.330. ISSN: 0360-3199.
[38] Shampine LF, Reichelt MW. The MATLAB code suite. SIAM J Sci Comput 1997;18(1):1–22.
[39] Byrne GD, Hindmarsh AC. Stiff ode solvers: a review of current and coming attractions. J Comput Phys 1987;70(1):1–62. https://doi.org/10.1016/0021-9991(87)90001-5. ISSN: 0021-9991.
[40] Younglove BA. Thermophysical properties of fluids. i. argon, ethylene, parahydrogen, nitrogen, nitrogen trifluoride, and oxygen. Journal of Physical and Chemical Reference Data 1982;11.
[41] C.H.J. van den Bosch, R.A.P.M. Weterings, "Methods for the calculation of physical effects, The. Yellow Book", The Director-General for Social Affairs and Employment, The Netherlands, 1997.